



1 Synergistic Use of Active and Passive Satellite Observations for 2 Monitoring Urban Fossil Fuel CO₂ Emission

3 Jinchun Yi ^{#,1}, Yiyang Huang ^{#,1}, Ge Han ^{*,1,3}, Hongyuan Zhang ², Zhipeng Pei ², Haotian Luo ¹, Yichi Zhang ¹,
4 Tianqi Shi ⁶, Siwei Li ^{1,3}, Wei Gong ^{4,5}

5 ¹Hubei Key Laboratory of Quantitative Remote Sensing of Land and Atmosphere, School of Remote Sensing and Information
6 Engineering, Wuhan University, Wuhan 430079, China.

7 ²State Key Laboratory of Information Engineering in Surveying, Mapping and Remote Sensing, Wuhan University, Luoyu Road
8 No.129, Wuhan 430079, China.

9 ³Perception and Effectiveness Assessment for Carbon-neutrality Efforts, Engineering Research Center of Ministry of Education,
10 Institute for Carbon Neutrality, Wuhan University, Wuhan, China.

11 ⁴Electronic Information School, Wuhan University, Wuhan, China.

12 ⁵Wuhan Institute of Quantum Technology, Wuhan, China.

13 ⁶Laboratoire des Sciences du Climat et de l'Environnement, LSCE/IPSL, CEA-CNRS-UVSQ, Université Paris-Saclay, 91198 Gif-
14 sur-Yvette, France.

15 *Correspondence to:* Ge Han (udhan@whu.edu.cn)

16 [#] These authors contributed equally to this work.

17 **Abstract.** Accurate estimation of fossil fuel CO₂ (ffCO₂) emissions is essential for climate prediction and the development of
18 mitigation policies. Top-down carbon - nitrogen joint observations offer the potential for more reliable ffCO₂ estimates. Here, we
19 establish an inversion framework for urban ffCO₂ emissions based on combined active-passive satellite observations. Urban ffCO₂
20 distributions were first constructed using satellite NO₂ data and CO₂-NO_x emission ratios, and monthly ffCO₂ emissions for selected
21 global cities were then estimated by integrating XCO₂ observations from the DQ-1 ACDL instrument. Our results show that satellite-
22 derived NO_x emissions provide strong constraints on urban anthropogenic CO₂ estimates. Validation against TCCON ground-based
23 observations indicates that, compared with conventional top-down inversion approaches, our method more accurately reproduces
24 urban ffXCO₂ plume distributions. We further evaluated the influence of different CO₂-NO_x ratio calculation methods on ffCO₂
25 estimates and found variations exceeding 150, exerting a substantial impact on emission inversions. Under observational constraints,
26 the uncertainty in CO₂-NO_x ratios derived from different methods decreased by 9.79 - 38.78%, and the variation range was reduced
27 by more than 100%, converging toward a consistent magnitude. This study advances understanding of the spatiotemporal patterns
28 of urban ffCO₂ emissions and provides a unified perspective for future CO₂-NO_x-based anthropogenic carbon emission estimation.



29 1. Introduction

30 The intensification of global climate change has driven an increasing demand for high-precision monitoring of fossil fuel CO₂
31 (ffCO₂) emissions(Agency 2009). The Paris Agreement emphasizes that countries need rapid and timely access to changes in carbon
32 emissions to support policy formulation and implementation. Achieving this goal relies on accurate and verifiable carbon accounting
33 systems. Cities, due to their high concentration of population, energy consumption, and economic activity, contribute over 70% of
34 global anthropogenic CO₂ emissions, making them key units for evaluating emission reduction policies and compliance
35 monitoring(Crippa et al. 2018). Existing global and regional emission inventories primarily adopt bottom-up statistical accounting
36 methods, estimating emissions based on energy production and sector-specific emission factors(Wei 2024; Xu et al. 2024). However,
37 these inventories often suffer from significant uncertainties due to data delays and incompleteness(Andres et al. 2012; Le Quéré et
38 al. 2018; Zhang et al. 2009).

39 To overcome the limitations of bottom-up approaches, top-down atmospheric inversion techniques have advanced rapidly in
40 recent years, enabling constraints on regional carbon budgets. Passive satellite remote sensing systems, such as GOSAT and OCO-
41 2/3, can invert XCO₂ over large portions of the globe and have unique potential for identifying local point sources, estimating
42 regional carbon fluxes, and inferring gross primary productivity(Eldering et al. 2017; Köhler et al. 2018; Li et al. 2018; Schwandner
43 et al. 2017; Sun et al. 2018b). Nonetheless, top-down inversion methods also rely on accurate prior emission estimates. Inventories
44 that downscale national or regional emissions to high spatial and temporal resolution often suffer from incomplete socio-economic
45 data and inaccurate emission conversion factors, leading to substantial uncertainties in urban emission estimates(Gately and Hutyrá
46 2017). Moreover, conventional top-down CO₂ inversion studies have focused primarily on quantifying terrestrial ecosystem carbon
47 fluxes, typically assuming fossil fuel emissions are known and unbiased. This complicates direct inference of anthropogenic
48 emissions from CO₂ observations due to the atmospheric mixing of fossil fuel and ecosystem fluxes(Ye et al. 2020).

49 Coupled carbon-nitrogen observations offer a new perspective to address this gap. Nitrogen oxides (NO_x = NO + NO₂) are
50 major co-emitted species from fossil fuel combustion, with emission intensity and spatial distribution closely correlated with
51 ffCO₂(Feng et al. 2024). Studies have shown that in regions with varying pollution levels, XCO₂ anomalies spatially correlate with
52 tropospheric NO₂ column densities(Hakkarainen et al. 2016). Moreover, the CO₂-to-NO_x ratio is often more stable than individual
53 emission amounts because systematic biases in fossil fuel consumption affect both CO₂ and NO_x statistics(Konovalov et al. 2016).
54 Recent research suggests that optimized NO_x emissions, combined with CO₂-to-NO_x ratios from bottom-up inventories, can provide
55 more accurate ffCO₂ estimates(Zheng et al. 2020). For instance, Zheng et al. used TROPOMI NO₂ data to estimate 10-day moving
56 averages of Chinese ffCO₂ emissions during the COVID-19 pandemic, finding an 11.5% decline compared to the same period in
57 2019(Zheng et al. 2020). Liu et al. validated the feasibility of NO_x-based ffCO₂ estimation by comparing inferred CO₂ emissions
58 with highly accurate stack measurements from eight large US power plant(Liu et al. 2020). High-resolution NO₂ column

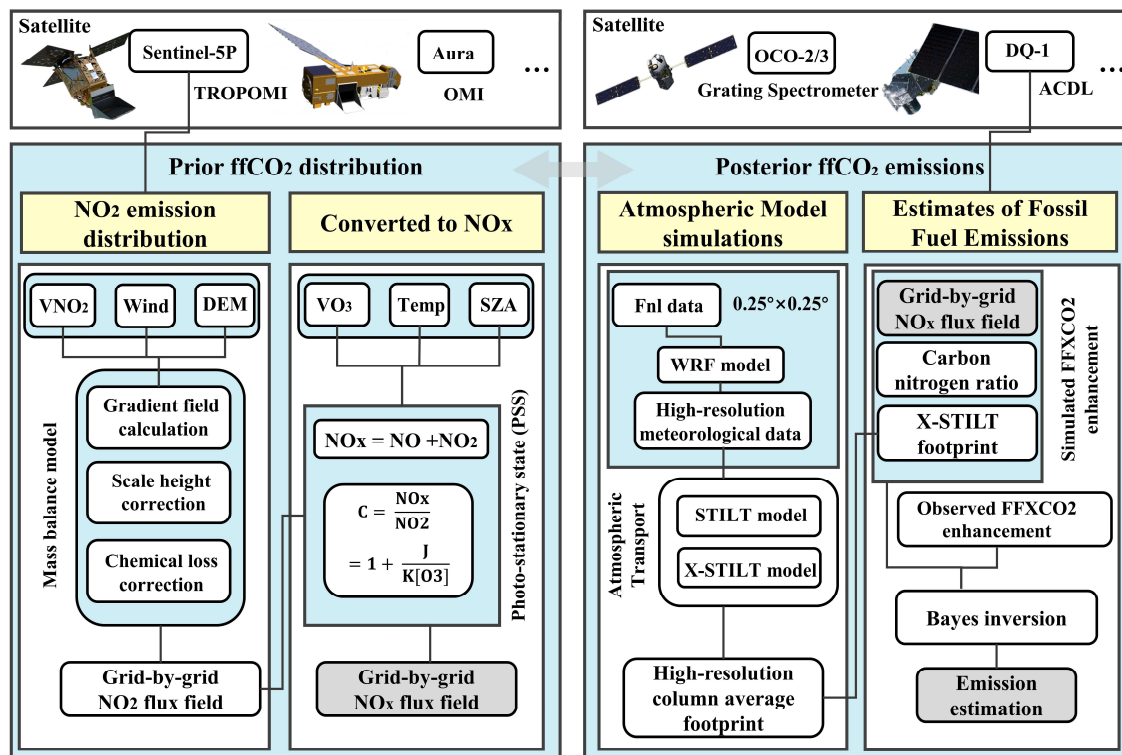


59 observations, such as those from Sentinel-5P/TROPOMI, can be inverted using a mass-balance framework to derive accurate NO_x
60 gridded fluxes (Beirle et al. 2023; Qin et al. 2023; Sun 2022; Sun et al. 2021). These NO_x fluxes can inform the prior spatial allocation
61 of CO_2 emissions due to the co-emission consistency of fossil fuel sources, and the high temporal resolution of TROPOMI allows
62 rapid updates of CO_2 priors, mitigating the lag inherent in static inventories (Zhang et al. 2022).

63 The CO_2 -to- NO_x ratio is crucial for converting NO_x emissions into ffCO_2 estimates. However, due to measurement limitations,
64 most studies derive this ratio from inventories, and different calculation methods yield significantly different values. Assimilating
65 observational data to invert CO_2 -to- NO_x ratios is therefore key to reducing uncertainties in ffCO_2 estimation. Passive top-down
66 observations are limited by cloud cover, aerosols, and solar irradiance, and in complex multi-source and topographic environments,
67 signal attribution is challenging, restricting the accuracy and stability of city-scale inversions (Miller et al. 2014).

68 In 2022, China launched DQ-1, the world's first CO_2 lidar satellite, equipped with an IPDA lidar (ACDL) capable of high
69 signal-to-noise ratio, day-and-night, all-weather observations. The dual-wavelength differential method mitigates interference from
70 aerosols and thin clouds (Han et al. 2017; Han et al. 2025). Compared to passive satellites, IPDA lidar offers unique advantages in
71 urban plume detection and fine-scale emission inversion (Kiemle et al. 2017; Kiemle et al. 2011; Yi et al. 2024). Previous studies
72 using DQ-1 XCO_2 data successfully constrained point-source emissions (Cheng et al. 2025; Han et al. 2024; Zhang et al. 2025), and
73 Yi et al. developed a kilometer-scale urban flux inversion system based on ACDL measurements, comparing its constraints to passive
74 systems like OCO-2/3 (Yi et al. 2024).

75 In this study, we propose a city-scale ffCO_2 inversion framework that jointly assimilates active and passive satellite observations,
76 dynamically bridging NO_x and CO_2 emissions via the CO_2 -to- NO_x ratio. The workflow is illustrated in Fig. 1. TROPOMI NO_2
77 column data are first used to invert NO_x gridded emissions via a mass-balance approach. Combined with prior CO_2 -to- NO_x ratios,
78 these NO_x fluxes are converted into CO_2 priors. DQ-1 XCO_2 -Lidar along-track measurements are then assimilated using WRF-
79 STILT high-resolution atmospheric transport simulations within a Bayesian inversion framework to estimate total city emissions
80 and explicitly quantify observational and transport uncertainties. We applied this approach to Beijing, Paris, and Cairo, representing
81 cities with diverse topographies and emission patterns, using August 2022 TROPOMI and DQ-1/ACDL data to evaluate the
82 framework's ability to provide robust, high-resolution urban emission estimates. It is noteworthy that no unified CO_2 -to- NO_x ratio
83 calculation method currently exists, and different methods yield divergent values, which can significantly bias final emission
84 estimates. This study systematically evaluates the influence of prior CO_2 -to- NO_x ratio calculation methods on inversion outcomes,
85 demonstrating that Bayesian assimilation can substantially reduce this uncertainty, converging different ratios to a consistent
86 magnitude. This framework offers a unified approach for estimating urban emissions under limited or uncertain inventory conditions,
87 providing a timely and reliable method for reporting anthropogenic CO_2 emissions at the city scale.



88
 89

Figure 1 Technical framework diagram

90 The remainder of this paper is structured as follows. Section 2 introduces the datasets and methods used in this study. Section
 91 3 presents the results of NO_x emission estimation in Paris, Cairo, and Beijing based on TROPOMI observations combined with a
 92 mass-balance approach, followed by city-scale ffCO₂ inversion results obtained by assimilating DQ-1 ACDL observations within a
 93 Bayesian framework. Section 4 examines the influence of different prior CO₂-to-NO_x ratio calculation methods on the inversion
 94 process and highlights the importance of optimizing the CO₂-to-NO_x ratio using observational data. Finally, Section 5 summarizes
 95 and discusses the potential of the multi-source satellite Bayesian inversion framework for constraining urban CO₂ emissions, and
 96 emphasizes the significance of optimized CO₂-to-NO_x ratios for improving the accuracy of urban ffCO₂ estimates.

97 **2. Materials and methods**

98 **2.1. Data**

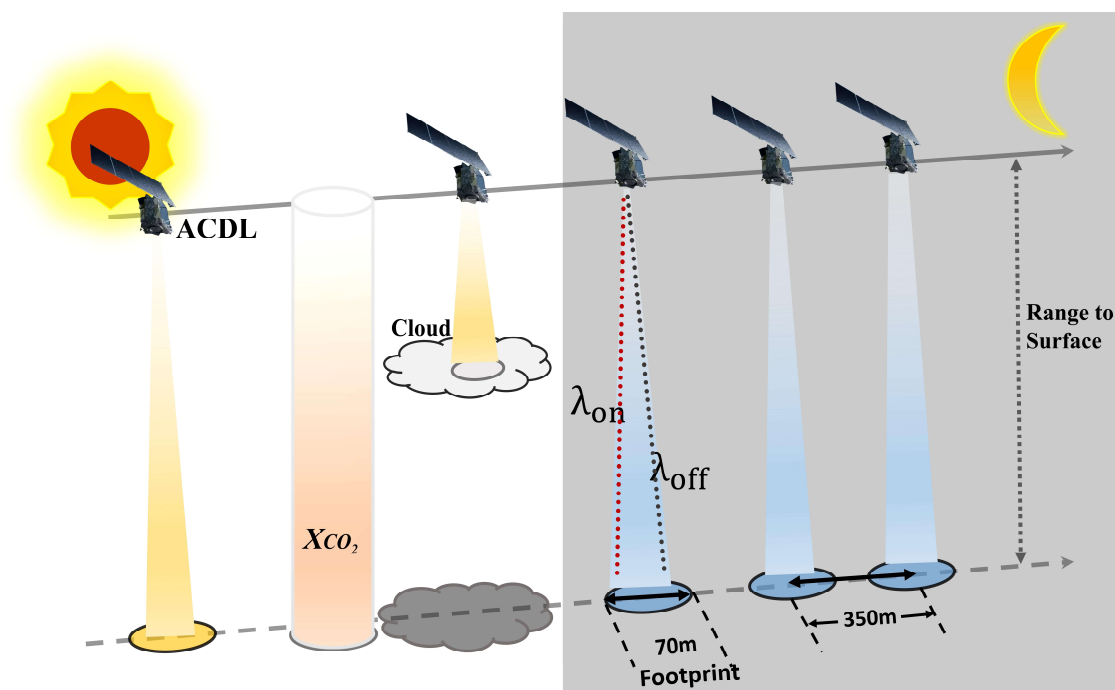
99 **2.1.1. ACDL Productions**

100 The concept of DQ-1 was first proposed in 2012 with the aim of developing a satellite-borne lidar system analogous to the
 101 Cloud-Aerosol Lidar with Orthogonal Polarization (CALIOP) onboard CALIPSO, and it was officially approved as a national



102 project in 2017. Unlike conventional environmental monitoring satellites, DQ-1 is distinguished by its breakthrough active remote
103 sensing payload—the Atmospheric Carbon Dioxide Differential Absorption Lidar (ACDL)—which enables direct “top-down”
104 observations of atmospheric CO₂. The ACDL underwent successive stages of laboratory prototype development and airborne
105 validation before its successful launch onboard the DQ-1 satellite into a near-polar sun-synchronous orbit at an altitude of ~705 km
106 on April 18, 2022. Operational observations commenced in late May of the same year. This study primarily analyzes data collected
107 August 2022.

108 The ACDL operates on the principle of Integrated Path Differential Absorption (IPDA) lidar, retrieving atmospheric column-
109 averaged CO₂ concentrations (X_{CO_2}) via differential absorption techniques. The inversion methodology and data product
110 specifications have been described in detail elsewhere; here, we provide only a brief overview (Han et al. 2025). The instrument
111 transmits two nearly simultaneous laser pulses: one at a strong absorption line of CO₂ (R16, referred to as the “online” wavelength)
112 and the other at a nearby weak absorption line (the “offline” wavelength). These are stabilized at 6361.225 cm⁻¹ and 6360.981 cm⁻¹,
113 corresponding to 1572.024 nm and 1572.085 nm, respectively. By comparing the differential attenuation between the online and
114 offline signals, the system effectively mitigates the influence of aerosols and other interfering species, except water vapor, thereby
115 enabling accurate retrievals of X_{CO_2} . The inversion process relies on dedicated algorithms, with the central concept being that the
116 small wavelength offset produces differential absorption, which enhances the sensitivity of CO₂ detection (details of the ACDL
117 X_{CO_2} retrieval algorithm are provided in the Appendix A1).



118

119 **Figure 2 the schematic diagram for DQ-1's detection principle**



120

121 Figure 2 illustrates the schematic of the DQ-1 measurement principle. The XCO₂ products generated by ACDL are provided in
122 a point-sampling mode analogous to that of GOSAT. The lidar records one footprint of approximately 70 m every ~350 m along the
123 satellite ground track. Additional details of the ACDL operating parameters are provided in the Appendix A1.

124 **2.1.2. TROPOMI Productions**

125 TROPOMI is a nadir-viewing spectrometer onboard ESA's Sentinel-5 Precursor (S5P) satellite, which was launched in October
126 2017. Operating in an ascending Sun-synchronous polar orbit with an equator crossing time of approximately 13:30 local time,
127 TROPOMI measures a range of trace gases as well as cloud and aerosol properties across four spectral channels (ultraviolet, visible,
128 near-infrared, and shortwave infrared). The instrument's minimum pixel size was about 3.5×7 km² at nadir before being reduced
129 to $\sim 3.5 \times 5.5$ km² on 6 August 2019 (Veefkind et al. 2012). In this study, we used the S5P-PAL dataset (consistent with version
130 2.3.1) (Eskes et al. 2021) covering the period from 1 August to 1 September 2022, obtained from <https://data-portal.s5p-pal.com>

131 To ensure data quality, we filtered out pixels with a qa_value < 0.75 (Qin et al. 2023), and, following van Geffen et al., removed
132 cloudy pixels (cloud radiance fraction > 50%) as well as anomalies (e.g., eclipses) from the TROPOMI NO₂ dataset (Van Geffen et
133 al. 2022). To test our algorithm framework on a robust dataset, we selected summer NO₂ observations for three cities located in the
134 mid-latitudes of the Northern Hemisphere, avoiding winter measurements that may be complicated by potential snow cover.
135 Furthermore, given the need for city-scale accuracy, air mass factor (AMF) corrections were applied locally following the method
136 described in (Beirle et al. 2023).

137 Sun et al. proposed an oversampling algorithm to project multi-satellite, multi-species observations onto a common grid, with
138 code publicly available on GitHub (https://github.com/Kang-Sun-CfA/Oversampling_matlab/) (Sun et al. 2018a). In this work, we
139 applied this algorithm to the pre-processed TROPOMI overpass data, generating oversampled grids at 1 km resolution following
140 the procedure described in (Sun 2022).

141 **2.1.3. Meteorological and DEM data**

142 For the estimation of CO₂ emissions through model simulations, we utilized meteorological parameters from the National
143 Centers for Environmental Prediction Final (NCEP FNL) operational global analysis dataset (National Centers for Environmental
144 Prediction/National Weather Service/NOAA/U.S. Department of Commerce, 2015). The ds083.3 dataset is provided on a $0.25^\circ \times$
145 0.25° latitude–longitude grid and updated every six hours via the Global Data Assimilation System (GDAS)
146 (<https://rda.ucar.edu/datasets/ds083-3/>). It covers 32 vertical levels, ranging from the surface to the top of the atmosphere, including
147 the ground level and 31 isobaric layers from 1000 hPa to 1 hPa. Essential variables such as surface pressure, geopotential height,
148 temperature, relative humidity, and zonal and meridional wind components were used as the main meteorological inputs for driving



149 the WRF-STILT simulations.

150 The wind vector data were obtained from the ERA5 reanalysis dataset (<https://doi.org/10.24381/cds.adbb2d47>)(Hersbach et al.
151 2023). We extracted hourly 10 m and 100 m wind vectors at 0.25° spatial resolution for the three selected cities during the period
152 from 1 August to 1 September 2022. The 10 m wind vectors are used to approximate near-surface winds, whereas the 100 m wind
153 vectors represent horizontal transport within the planetary boundary layer. These data were averaged to daily values and
154 subsequently interpolated to match the grid resolution of the column concentration fields described in Section 2.3.1.

155 Digital elevation data were obtained from the GMTED2010 dataset (<https://www.usgs.gov/coastal-changes-and-impacts/gmted2010>)(Danielson and Gesch 2011). The DEM was resampled and mapped to the same spatial grid as the concentration
156 and wind fields to ensure consistency across all datasets.
157

158 **2.1.4. Emissions Inventory**

159 In this study, multiple emission inventories were used to estimate fossil fuel CO₂ (ffCO₂) emissions and to calculate the CO₂-
160 to-NO_x ratio. In the urban observation system simulation experiment (Section 3), the GEMS inventory (0.1° resolution) for NO_x and
161 CO₂ emissions(Huang et al. 2017; Wang et al. 2013) was used to derive the prior CO₂-to-NO_x ratio (available at:
162 <https://gems.sustech.edu.cn/data>). For comparison, we also employed the gridded fossil fuel CO₂ emissions inventory from the
163 Open - source Data Inventory for Atmospheric Carbon dioxide (ODIAC, Version 2024, 1 km resolution;
164 <https://db.cger.nies.go.jp/dataset/ODIAC/>)(Oda and Maksyutov 2015). In Section 4, we further utilized the sectoral and 0.1° gridded
165 NO_x and CO₂ inventories from the Emissions Database for Global Atmospheric Research (EDGAR;
166 https://edgar.jrc.ec.europa.eu/emissions_data_and_maps)(Crippa et al. 2018), as well as the sectoral NO_x and CO₂ inventories from
167 the Multi-resolution Emission Inventory model for Climate and air pollution research (MEIC; <http://meicmodel.org.cn/>)(Team 2012).
168 Using different approaches to calculate the CO₂-to-NO_x ratio, we quantified the variations arising from different inventory inputs
169 and assessed their impact on emission inversions.

170 **2.2. Methodology**

171 **2.2.1. Calculation of Prior Distribution for CO₂ Emissions**

172 **(1) Mass Balance Method**

173 In previous studies, numerous works have detailed the theoretical derivation for inferring gridded fluxes from column
174 observations(Beirle et al. 2023; Huang et al. 2024; Koene et al. 2024; Qin et al. 2023; Rey-Pommier et al. 2025; Sun et al. 2018a).
175 Such frameworks are generally based on solutions to the atmospheric continuity equation. Divergence-based approaches typically
176 rely on several key assumptions: (1) exchanges above the planetary boundary layer (column top) and at the surface (column bottom)



177 are neglected, effectively assuming two-dimensional diffusion; (2) horizontal turbulent transport is ignored at coarse grid resolutions;
178 and (3) the deposition term S is treated using a first-order chemical approximation. Starting from the unsteady, source-driven
179 atmospheric continuity equation, the gridded flux of a given species, such as NO_2 , can be derived from satellite column observations,
180 with the resulting flux $\langle E_{\text{NO}_2} \rangle$ expressed as in Equation 1.

$$181 \quad \langle E_{\text{NO}_2} \rangle = \langle \vec{u} \cdot (\nabla V_{\text{NO}_2}) \rangle + \frac{\langle V_{\text{NO}_2} u_{10} \cdot (\nabla z_0) \rangle}{H} + \frac{\langle V_{\text{NO}_2} \rangle}{\tau} \quad (1)$$

182 The detailed derivation is provided in Appendix A2. To fully exploit the available data while accounting for observational
183 errors, spatial gradients were computed along the zonal, meridional, and both diagonal directions. Gradients were numerically
184 approximated using second-order central differences, multiplied by the corresponding decomposed wind vectors, and then averaged.
185 For boundary grid points, one-sided differences were applied.

186 (2) Convert NO_2 to NO_x

187 Nitrogen oxides ($\text{NO}_x = \text{NO} + \text{NO}_2$) do not exist independently in the troposphere, as NO and NO_2 continuously interconvert,
188 while the total NO_x remains relatively stable. To convert between NO_2 column densities and total NO_x columns, Sun et al. applied a
189 fixed coefficient of 1.32. In this study, we adopt a more rigorous approach to derive the conversion factor, as expressed in Equation
190 2(Beirle et al. 2023), based on the photostationary steady-state assumption:

$$191 \quad \begin{cases} V_{\text{NO}_x} = \alpha V_{\text{NO}_2} = \left(1 + \frac{J}{K X_{\text{O}_3}}\right) V_{\text{NO}} \\ J = k_1 * \exp\left(-\frac{k_2}{\cos(\text{SZA})}\right) \\ K = k_3 * \exp\left(-\frac{k_4}{T}\right) \end{cases} \quad (2)$$

192 Here, J represents the photolysis frequency of NO_2 , calculated following the methodology in (Dickerson et al. 1982). The rate
193 constants k_1 and k_2 are set to 0.0167 and 0.575, respectively. The solar zenith angle (SZA) can be directly determined from the
194 local latitude, longitude, and time; in this study, SZA values are obtained from the TROPOMI satellite metadata. K denotes the
195 chemical reaction rate constants for NO with O_3 , expressed in $\text{cm}^3/(\text{mol}\cdot\text{s})$ and recommended by IUPAC, with $k_3=2.07*10^{-12}$ and
196 $k_4=1400$. The ozone mixing ratio, X_{O_3} , is derived from the ESCiMo project (Brenninkmeijer and Cai 2016), and T represents the
197 boundary-layer mean temperature obtained from ERA5 reanalysis data. Under these definitions, Equation 2 can be rewritten as:

$$198 \quad X = \alpha * \langle E_{\text{NO}} \rangle \quad (3)$$

199 Using Equation 3 we can obtain grid-resolved estimates of NO_x fluxes, which serve as the prior distribution for fossil fuel CO_2
200 (ffCO_2) emissions. These estimates provide a data-driven prior inventory for subsequent steps in the inversion framework.



201 **(3) Scale height and Chemical lifetime**

202 Regarding the selection of scale height and first-order chemical lifetime, previous studies, such as Beirle et al., employed fixed
203 empirical scale height values and adjusted terrain correction terms to obtain optimal estimates(Beirle et al. 2023). Their chemical
204 lifetime was calculated using a compensation method that accounted for losses integrated over residence times within a 15 km buffer.
205 While effective at point-source scales, this approach is not directly applicable to our study. In the present work, we follow Sun et
206 al.'s purely data-driven approach, which leverages observational data without introducing additional assumptions, constructing a
207 linear regression model to determine these parameters(Sun 2022). This observation-driven fitting method not only reduces errors
208 arising from new assumptions but also mitigates biases caused by grid resampling and near-surface wind selection.

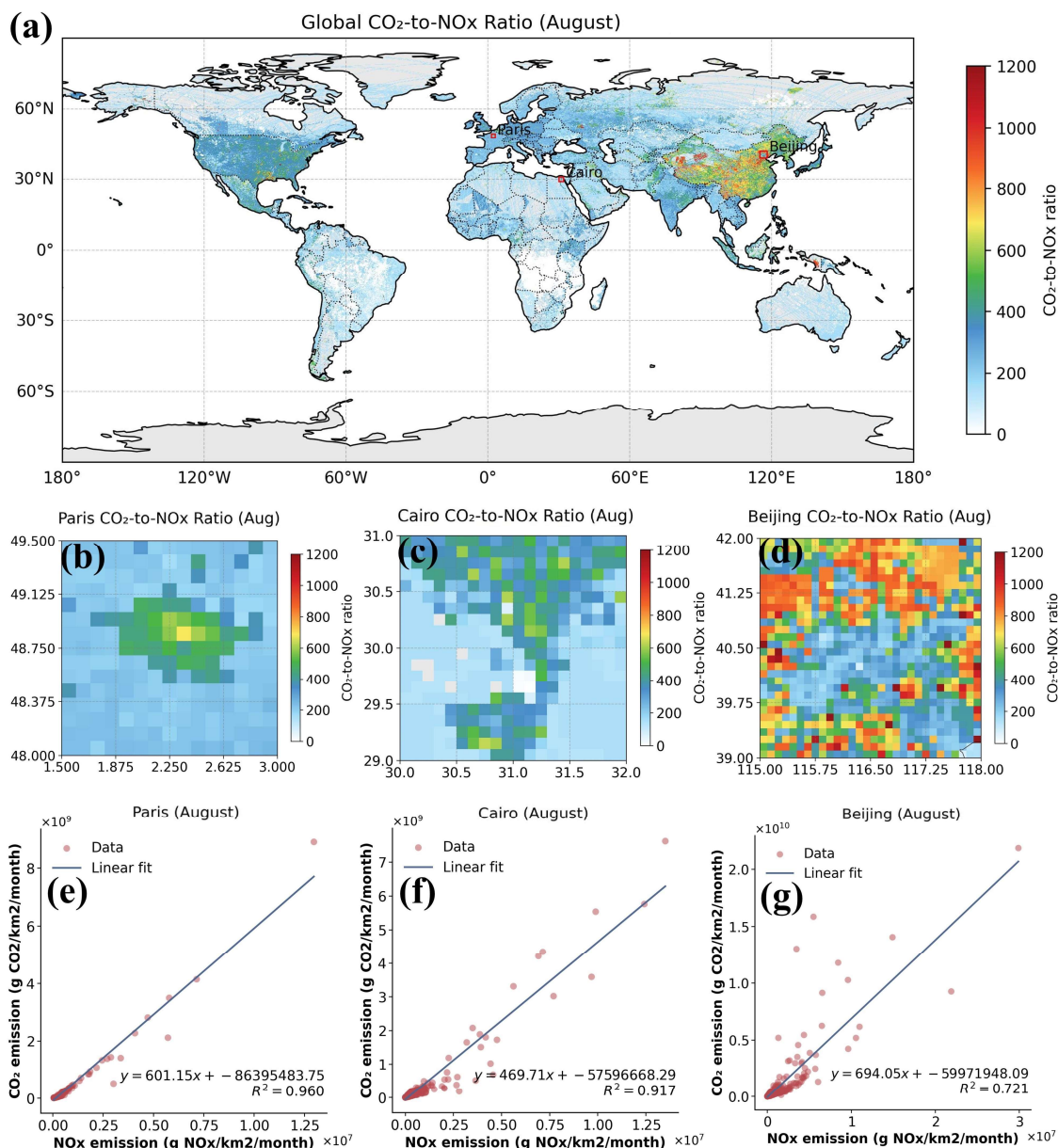
209 To suppress excessive noise in single-day fits, we perform monthly regressions and adopt the temporal and spatial mean over
210 the month as the final estimate, representing an aggregate over the full spatial domain, the entire month, and the troposphere. The
211 retrieved scale height and first-order chemical lifetime are then applied back into Equations 4 and 6 to obtain the final gridded NO_x
212 vertical fluxes.

213 After terrain correction, the gridded flux fields remove a substantial portion of strong emission signals obscured by wind
214 divergence and negative divergence artifacts, while the chemical correction term adjusts residual minor negative biases(Beirle et al.
215 2023; Sun 2022; Sun et al. 2018a). Any remaining small negative values after these corrections are set to zero.

216 **(4) Calculation of Prior CO₂-to-NO_x Ratio**

217 We used the prior CO₂-to-NO_x ratio in combination with TROPOMI-derived NO_x emission distributions to obtain an initial
218 characterization of urban prior ffCO₂ emissions. Following the approach of Feng et al., who calculated the CO₂-to-NO_x ratio by
219 dividing gridded CO₂ and NO_x emission inventories(Feng et al. 2024), we derived city-specific prior CO₂-to-NO_x ratio using the
220 0.1° CO₂ and NO_x inventories from GEMS (<https://gems.sustech.edu.cn/data/database>). Unlike Feng et al., who focused on grid-
221 level CO₂-to-NO_x ratio, we fitted the gridded ratios across each study region to obtain an integrated city-level CO₂-to-NO_x ratio,
222 which is more suitable for subsequent inversion analyses (Fig. 3). Details on the associated uncertainties are provided in Section
223 4.1.

224 Figure 3 illustrates our method for calculating the prior CO₂-to-NO_x ratio. By fitting the 0.1° gridded ratios for each city, we
225 obtained overall city-scale values. The coefficients of determination (R²) for Paris, Cairo, and Beijing were 0.96, 0.917, and 0.76,
226 respectively.



227
 228 **Figure 3** Schematic diagram of prior CO₂-to-NO_x ratio calculation methods. Panel (a) shows the global gridded CO₂-to-NO_x ratio derived
 229 from GMES data. Panels (b)–(d) present the gridded CO₂-to-NO_x ratio for Paris, Cairo, and Beijing. Panels (e)–(g) display the overall
 230 CO₂-to-NO_x ratio fitting results for the three cities.

231 **2.2.2. Estimating ffCO₂ emissions by WRF-STILT simulations**

232 **(1) Quantifying ffXCO₂ enhancements**

233 Distinguishing anthropogenic emission signals from the surrounding “clean” background in XCO₂ observations is a central



234 challenge for constraining urban carbon emissions via satellite. Definitions of “background” vary across studies. In this work, we
 235 define the background as atmospheric XCO₂ that is unaffected by local emissions within the study region. Following the approach
 236 proposed by (Ye et al. 2020) in constraining urban emissions using OCO-2 observations, we adopt a baseline calculation strategy
 237 that incorporates latitudinal gradients.

238 In this framework, XCO₂ is decomposed into two components: $XCO2_{trend}$, representing the regional-scale, non-local trend,
 239 and $XCO2_{local}$, whose standard deviation σ_{local} characterizes local-scale variability. Samples satisfying $XCO2 < XCO2_{trend} +$
 240 $0.5\sigma_{local}$ are selected as “background samples,” as they exhibit lower local spatial variability compared with data influenced by
 241 fossil fuel emissions. These background samples are then subjected to linear regression to derive the background baseline and
 242 characterize its spatial variation.

243 (2) X-Stochastic Time-Inverted Lagrangian Transport model for ACDL productions

244 We employ the X-STILT V1 model to trace CO₂ concentration variations driven by prior emission information. X-STILT
 245 integrates satellite profile data and enables a comprehensive uncertainty assessment of urban XCO₂ enhancements on a per-
 246 observation basis (Wu et al. 2018). Originally developed to extract urban signals from passive OCO-2 XCO₂ observations, we have
 247 adapted the framework for use with the active CO₂ satellite DQ-1, with appropriate modifications. The relationship between
 248 XCO₂^{Lidar} measurements and the CO₂ vertical profile, CO₂(p), can be formulated as follows:

$$249 \quad XCO2^{Lidar} = \frac{\int_{p_{surface}}^{p_{toa}} CO2(p)WF(p)dp}{\int_{p_{surface}}^{p_{toa}} WF(p)dp} = \sum_{n=1}^{toa} \frac{WF(p_n)}{IWF} \cdot CO2(p_n) \quad (4)$$

250 We approximate the CO₂ concentration by summing the background concentration with the simulated ffCO₂ enhancement.
 251 Here, the simulated ffCO₂ enhancement, $\Delta CO2_{ffCO2}(p) = \langle ffCO2, foot(p) \rangle$, is obtained by interpolating the modeled ffCO₂
 252 fluxes along tracer-tagged footprints. Consequently, the relationship between the ffCO₂ fluxes and the simulated $XCO2_{mod}^{Lidar}$, is
 253 established, yielding the modeled fossil fuel CO₂ enhancement $XCO2_{ffCO2, mod}^{Lidar}$ along the lidar track:

$$254 \quad XCO2_{ffCO2, mod}^{Lidar} = XCO2_{mod}^{Lidar} - XCO2_{background}^{Lidar} = \sum_{n=1}^{toa} \frac{WF(p_n)}{IWF} \cdot \langle emissions, foot(p_n) \rangle \quad (5)$$

255 $XCO2_{background}^{Lidar}$ represents the background concentration along the selected DQ-1 orbit (see Section 2.2.2 (1)). The operator
 256 \langle, \rangle denotes an inner product, ffCO₂ is the prior emission flux, and $foot(p_n)$ represents the modeled footprint at different vertical
 257 layers. Using the above formulation, the mathematical foundation for the inversion is established. By integrating footprints across
 258 multiple release heights, the equation can be further simplified. In this study, we define the ffXCO₂ enhancement simulated via the
 259 atmospheric transport model as:

$$260 \quad XSTILT^{Lidar} = \sum_{n=1}^{toa} \frac{WF(p_n)}{IWF} \cdot foot(h_n) \quad (6)$$



$$261 \quad XCO2_{ffCO2,mod}^{Lidar} = \langle XSTILT^{Lidar}, emissions \rangle \quad (7)$$

262 Here, $XSTILT^{Lidar}$ is defined as the column-averaged footprint, corresponding to the column-averaged CO₂ concentration.
 263 The inner product of the column-averaged footprint and the prior emission flux yields the simulated XCO₂ enhancement.

264 (3) Bayes inversion

265 We used the NO_x emissions obtained previously as prior fluxes and, through the CO₂-to-NO_x ratio, established the relationship
 266 between the prior emissions and the XCO₂ observed by DQ-1 (Equation 9). The XCO₂ enhancements estimated from DQ-1
 267 observations were then employed to impose “top-down” constraints on the simulated results. Following the approaches of (Che et
 268 al. 2024; Sheng et al. 2025; Wang et al. 2014; Ye et al. 2020), we applied a Bayesian inversion framework to optimize the prior
 269 emission estimates.

$$270 \quad y_{obs} = y_{sim} \cdot \lambda + \varepsilon_p \quad (8)$$

271 Here, y_{obs} and y_{sim} represent the observed ffXCO₂ enhancements and the simulated NO_x enhancements, respectively. The
 272 symbol λ denotes the CO₂-to-NO_x ratio, and ε_p represents the observational error, which encompasses contributions from DQ-1
 273 measurement uncertainties, model errors, and errors in model parameters. It is defined as follows:

$$274 \quad \begin{cases} y_{obs} = \int_{latitude1}^{latitude} ffXCO2_{obs} dt \\ y_{sim} = \int_{latitude1}^{latitude2} \langle X, footprint \rangle dt \end{cases} \quad (9)$$

$$275 \quad \varepsilon_{obs} = \sqrt{\sigma_{measurement}^2 + \sigma_{sim}^2} \quad (10)$$

276 In this context, ffXCO_{2,obs} represents the DQ-1 XCO₂ enhancement after background concentration removal. The notation \langle
 277 $X, footprint \rangle$ denotes the simulated NO_x enhancement, obtained by convolving the NO_x emission inventory X with the STILT-
 278 derived footprint. Pseudo-observations, ffXCO_{2,obs}, are generated by averaging DQ-1 measurements over one-second intervals along
 279 the satellite track (~7 km), together with the corresponding simulated values.

280 Following the Bayesian inversion approach, the state vector λ is expressed in terms of the CO₂-to-NO_x ratio, representing the
 281 relationship between urban fossil fuel CO₂ and NO_x emissions. The Jacobian matrix is derived from the simulated NO_x enhancement
 282 y_{sim} . Here, $\sigma_{measurement}^2$ represents the observational error variance, and σ_{sim}^2 denotes the model transport error variance. DQ-1
 283 observations are assumed unbiased with respect to the true state. To account for measurement uncertainty, random Gaussian noise
 284 with a standard deviation of 0.3 ppm—representing the lower limit of observational error—is added to the observations.

285 By minimizing the loss function, we obtain the posterior CO₂-to-NO_x ratio $\hat{\lambda}$ and posterior uncertainty $\hat{\sigma}$:

$$286 \quad \hat{\lambda} = \lambda + \sigma_{sim}^2 y_{sim}^T (y_{sim} S_{obs} y_{sim}^T + S_{obs})^{-1} (y_{obs} - y_{sim} \lambda) \quad (11)$$



287
$$\hat{\sigma}^2 = (y_{sim}^T S_{obs}^{-1} y_{sim} + \sigma_{sim}^{-2})^{-1} \quad (12)$$

288 Here, the prior uncertainty σ_{sim} is primarily derived from the uncertainties in the prior NO_x emission distribution σ_{NO_x} and
289 the prior CO₂-to-NO_x ratio $\sigma_{C/N}$ as equation 13:

290
$$\sigma_{sim} = \sqrt{\sigma_{NO_x}^2 + \sigma_{C/N}^2} \quad (13)$$

291 3. Urban Observation System Simulation Experiment

292 3.1. Satellite-driven urban NO_x emission distribution

293 As described in Section 2.2.1, we applied the mass balance approach in the three cities to derive prior NO_x gridded inventories,
294 which serve as the basis for constructing ffCO₂ gridded emissions. The grid resolution was set to 5 km × 5 km. Figure 4 illustrates
295 the detailed NO_x fluxes for August 2022 over Beijing, Paris, and Cairo, produced entirely via a top-down approach, with panels (a)–
296 (c) corresponding to Beijing, Paris, and Cairo, respectively.

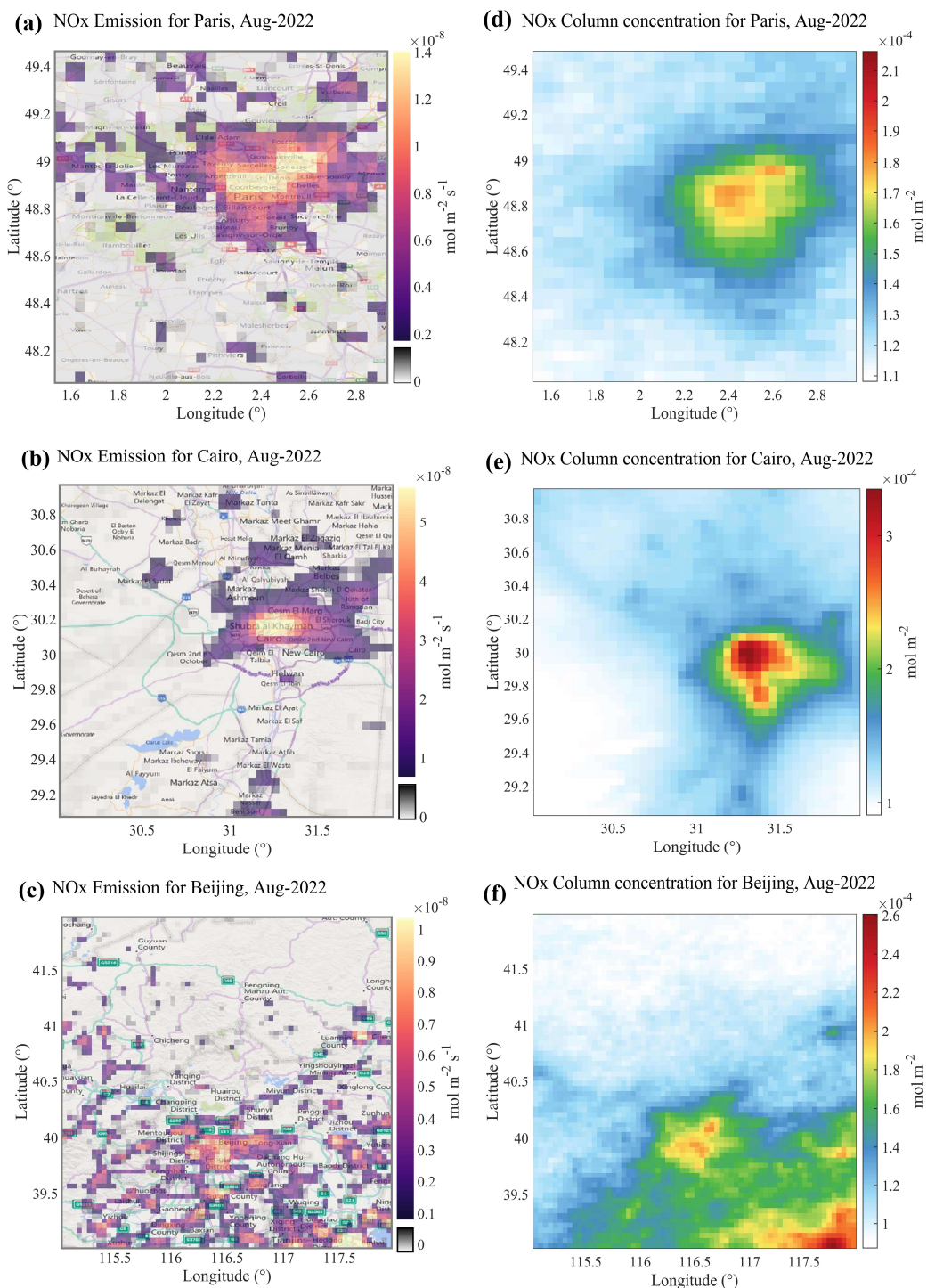
297 From the figure, it is evident that the average NO_x flux magnitude in all three cities is on the order of ~10⁻⁸ mol m⁻² s⁻¹. However,
298 their spatial distributions differ considerably. Both Paris and Cairo exhibit highly concentrated emission patterns. In Cairo, the
299 central urban area and industrial zones display peak NO_x fluxes on the order of ~10⁻⁷ mol m⁻² s⁻¹. These high-flux regions sharply
300 decrease with distance from the center, highlighting a pronounced urban boundary effect. In contrast, Beijing not only exhibits
301 strong emissions in the central urban area (within the Sixth Ring Road) but also features numerous dispersed point- and area-like
302 sources in suburban districts (e.g., Fangshan in the southwest) and in the surrounding hills and mountains. Compared with Cairo's
303 concentrated emissions, Beijing's peak NO_x grid flux in the urban core is nearly one order of magnitude lower (see the color scale
304 mapping in Fig. 4); however, due to the city's larger spatial extent, the total flux remains substantially higher than that of Cairo.

305 Beijing's topography, with higher elevations in the northwest and lower elevations in the southeast, can induce local wind
306 divergence over hilly and mountainous areas. This effect may generate false positives when using the divergence method (Liu et al.
307 2021; Sun et al. 2021). In the northwestern suburban mountains of Beijing, the mean wind divergence can reach magnitudes of ~
308 ± 10⁻⁴ s⁻¹, while TROPOMI NO₂ column densities are on the order of 10⁻⁴ mol m⁻². Such magnitudes are comparable to mid-scale
309 urban averages or point-source emissions. Neglecting the divergence term can result in genuine emissions being omitted, while
310 background fluxes induced by terrain or wind divergence are mistakenly included. Following (Sun 2022), we applied Eq. A5 to
311 reconstruct the wind-divergence term using surface wind and terrain gradients, thereby reintegrating previously neglected area-like
312 emissions. Using Beirle et al.'s methodology, we integrated the net gridded fluxes within a 60 km radius centered on Beijing over
313 the entire year of 2022 to estimate the city's annual NO_x emissions at 251,450 t. This value is approximately 9.7% higher than the



314 2022 annual emission reported in the MEIC inventory for Beijing (227,000 t). Although the total magnitude is consistent, the spatial
315 distribution from top-down estimates differs substantially from bottom-up inventories. Section 3.2.2 further analyzes these
316 differences by simulating urban ffCO₂ plumes using both our ffCO₂ inventory and the ODIAC inventory.

317 By comparison, Paris and Cairo are situated on relatively flat terrain (maximum elevation ~180 m). Terrain-induced wind
318 divergence is negligible relative to total fluxes (wind-terrain and divergence contributions $\sim 10^{-10}$ mol m⁻² s⁻¹), leaving the continuity
319 equation primarily governed by wind-weighted column gradients. Cairo, located upstream of the Nile Delta in a high-albedo desert
320 region, benefits from low uncertainty in satellite-derived NO₂ columns. Under these conditions, the top-down NO_x inventory closely
321 aligns with the bottom-up inventory in terms of spatial distribution. Paris, situated in the Paris Basin along the Seine River,
322 experiences minimal terrain gradients. Although less extreme than Cairo, the slight topographic variation still produces pronounced
323 urban boundary effects in the inversion results.



324
 325 **Figure 4** Gridded prior NO_x emission inventories derived from the mass balance method. Panels (a)–(c) show the NO_x flux distributions
 326 (unit: mol/m²/s) for Beijing, Paris, and Cairo in August 2022. Panels (d)–(f) present the resampled monthly mean NO₂ column



327 concentration distributions for the three cities. Basemap for panels (a)–(c): Esri World Topographic Map. Sources: Esri, HERE, Garmin,
328 Intermap, INCREMENT P, GEBCO, USGS, FAO, NPS, NRCAN, GeoBase, IGN, Kadaster NL, Ordnance Survey, Esri Japan, METI,
329 Mapwithyou, NOSTRA, © OpenStreetMap contributors, and the GIS user community.

330

331 To quantitatively compare the NO_x emission characteristics and atmospheric behavior among Beijing, Paris, and Cairo, derived
332 using the mass balance approach, we analyzed key parameters for August, including mean NO_x fluxes, total emissions, chemical
333 lifetimes, vertical distribution scale heights, and NO_x/NO₂ ratios (Table 1). These NO_x behavior parameters reflect heterogeneous
334 characteristics shaped by the interplay of emission intensity, photochemical conditions, and boundary layer structure.

335 In terms of mean NO_x flux per unit area (mol m⁻² s⁻¹), Cairo exhibits the highest value (0.35 × 10⁻⁸), followed by Paris (0.28 ×
336 10⁻⁸) and Beijing (0.24 × 10⁻⁸), indicating a higher concentration of urban emission sources in Cairo—particularly from traffic—
337 resulting in stronger NO_x release per unit surface area. Nevertheless, Beijing’s total NO_x emissions (182,800 t yr⁻¹) are substantially
338 higher than those of the other two cities, reflecting its larger urban extent and greater overall emission intensity, characteristic of a
339 complex multi-source emission profile.

340 The first-order chemical lifetime of NO_x in the atmosphere indicates its removal rate and is influenced by factors such as OH
341 radical concentration and solar radiation intensity. Paris exhibits the longest NO_x chemical lifetime (6.91 h), followed by Beijing
342 (4.70 h) and Cairo (2.93 h). These differences are closely linked to photochemical activity: strong summer sunlight and high
343 temperatures in Cairo enhance OH-driven removal reactions, whereas the relatively mild mid-latitude climate of Paris, combined
344 with emission control measures, prolongs NO_x lifetime.

345 Regarding vertical distribution, the NO_x scale height also varies across the three cities. Beijing shows the highest scale height
346 (2.08 km), reflecting the combined effects of strong convective transport and multi-source emissions that elevate NO_x into the upper
347 mixing layer. By contrast, Cairo (1.41 km) and Paris (1.21 km) display more typical boundary-layer-constrained distributions,
348 indicating that ground-level emission controls and thermal structure strongly modulate vertical NO_x transport.

349 Finally, the NO_x/NO₂ ratio provides insight into the proportion of NO and its degree of conversion. Beijing exhibits the highest
350 ratio (1.41), followed by Cairo (1.32) and Paris (1.29), suggesting a higher fraction of NO in Beijing, likely associated with dense
351 traffic sources and a larger fraction of primary NO emissions. The relatively lower ratio in Paris reflects a higher NO₂ fraction,
352 consistent with effective emission controls and extensive photochemical conversion.

353

354 **Table 1** Grid-averaged NO_x fluxes, with total urban NO_x emissions as intermediate parameters in the mass balance method.

City	NO _x average flux mol/(m ² * s)	NO _x total emission kt/month	Chemical lifetime(hour)	Scale height(km)	NO _x /NO ₂
Beijing	0.235 10 ⁻⁸	15.29	4.69	2.07	1.41



Paris	$0.277 \cdot 10^{-8}$	4.45	6.90	1.21	1.29
Cairo	$0.353 \cdot 10^{-8}$	6.78	2.93	1.40	1.32

355

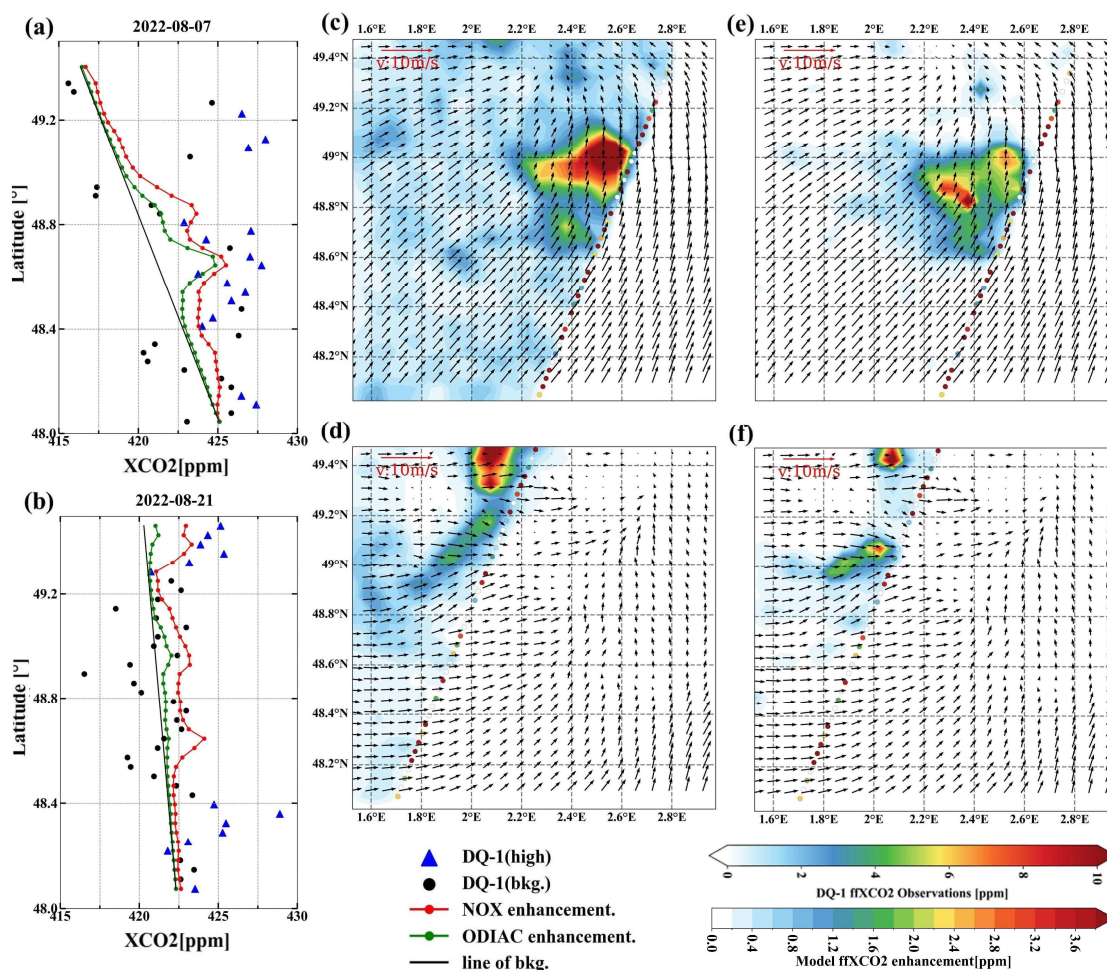
356 3.2. Urban Fossil Fuel XCO₂ Enhancement (ffXCO₂)

357 In this section, we summarize the prior ffXCO₂ emissions for each study region. For the selected orbits, the total monthly
358 emissions of Beijing, Paris, and Cairo were approximately 7.47–9.94, 2.91–3.33, and 2.73–3.60 MtC/month, respectively. To
359 constrain emissions, we compared observed and simulated ffXCO₂ enhancements, where ffXCO₂ enhancement is defined as the
360 increase in XCO₂ relative to the background level caused by local fossil fuel emissions. The prior ffXCO₂ enhancements were
361 simulated by taking the inner product of prior NO_x emissions inventories with STILT footprints, while the observed enhancements
362 from DQ-1 were derived by subtracting the background concentration from the measured XCO₂. By comparing prior and observed
363 ffXCO₂ enhancements, we assessed the variability of ffXCO₂ along the orbit and investigated the sources and detectability of the
364 ffXCO₂ signal.

365 3.2.1. Comparison of Modeled and Observed ffXCO₂

366 Complex horizontal wind fields can lead to elongated and non-Gaussian plume structures in simulated ffXCO₂ distributions (Ye
367 et al. 2020). This feature is illustrated in Fig. 5c–f. Figures 5a and 5b show the simulated and observed XCO₂ along two overpasses
368 (simulated XCO₂ is obtained by adding the simulated ffXCO₂ to the background derived in Section 2.2.2 (1)). Along these overpasses,
369 ffXCO₂ enhancements exceeding 5 and 10 ppm were observed, with the measured enhancements consistently larger than the
370 simulated values. Although the simulated peak on 7 August is narrower than the observed peak, and the observed peak near 48.4°
371 on 21 August shows a ~0.3° displacement relative to the simulation, the overall magnitude of simulated ffXCO₂ agrees well with
372 observations.

373 To further evaluate the feasibility of constraining fossil fuel CO₂ emissions using the NO_x inventory, we performed a
374 comparative analysis using the ODIAC inventory. We compared simulated ffXCO₂ during the satellite overpasses based on the NO_x
375 and ODIAC inventories (colored shaded areas in the figure), as well as their contributions to the pseudo-observed XCO₂ at the
376 satellite locations (colored dots), where the red line represents enhancements derived from the NO_x inventory and the green line
377 represents those from ODIAC. Over Paris, the NO_x-based simulation yields higher ffXCO₂ enhancements than ODIAC, likely due
378 to uncertainty in the prior CO₂-to-NO_x ratio. Nonetheless, both inventories capture enhancements exceeding 4 ppm. Moreover, the
379 line plots indicate that the temporal variation and magnitude of the simulated concentration contributions (red and green lines) are
380 nearly identical.



381
 382 **Figure 5** Comparison between simulated and observed ffxCO₂ enhancements using DQ-1 overpasses above Paris on 7 August 2022 and
 383 21 August 2022 at 01:00 UTC. Panels (a) and (b) show DQ-1 XCO₂ along the two tracks (black dots and blue triangles) and simulated
 384 XCO₂ (red solid line: sum of background concentration and ffxCO₂ simulated using the NO_x emissions; green solid line: sum of
 385 background concentration and ffxCO₂ simulated using the ODIAC inventory), averaged over 0.5 s. Black circles denote the data used to
 386 derive the background concentration (black solid line). Panels (c)–(f) show simulated ffxCO₂ and observed ffxCO₂ retrieved from DQ-1
 387 data ((c), (d): based on the NO_x inventory; (e), (f): based on the ODIAC inventory). Background XCO₂ concentrations have been subtracted.
 388 The reference vector indicates a wind speed of 10 m/s.

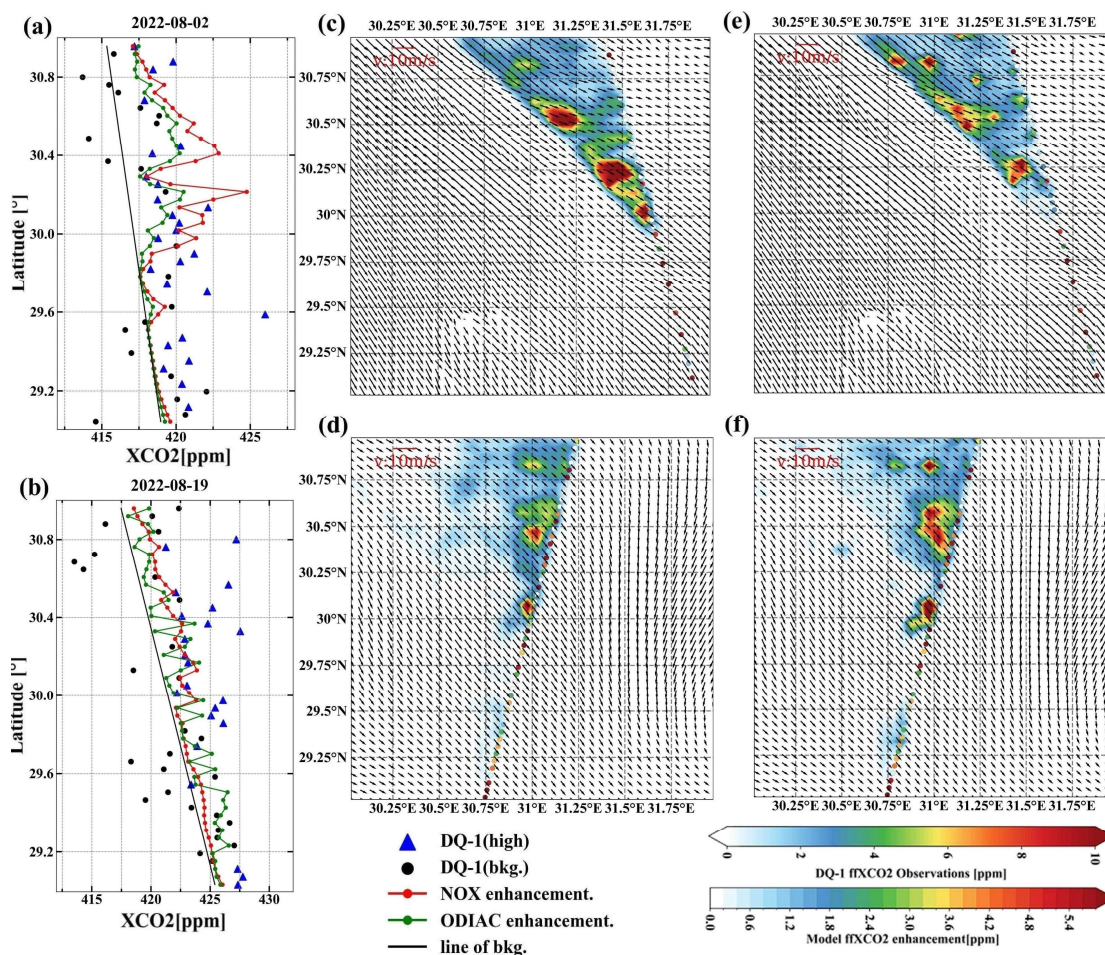
389

390 We examined local ffxCO₂ enhancements during two overpasses of Cairo on 2 August 2022 at 11:00 and 19 August 2022 at
 391 23:00. As shown in Fig. 6, the simulated ffxCO₂ peaks exceed 6 ppm. In contrast to Paris, where enhancements are widespread,
 392 diffuse, and lack clear structure, and Beijing, where plumes exhibit complex patterns, the simulated ffxCO₂ over Cairo is strongly
 393 influenced by northwesterly winds, resulting in well-defined plumes. Figure 5a illustrates that the simulations based on both
 394 inventories on 2 August produce similar magnitudes and trends, consistent with the Paris results, where the NO_x-based simulation



395 exceeds that from ODIAC. Notably, the simulated peaks on 2 August also show a spatial offset relative to the observations.
 396 Following Ye et al. 2020, such offsets are attributed to the satellite trajectory crossing the plume edges nearly parallel to the plume
 397 axis, making the simulated fFXCO₂ highly sensitive to errors in the horizontal wind field.

398 Notably, the overpasses above Paris and Cairo (Figs. 5a and 6b) exhibit higher latitudinal gradients in the background XCO₂,
 399 as indicated by the background lines. The approach used to derive these background lines provides a reliable estimate of background
 400 XCO₂ because, within the relevant regions, the observed and modeled cumulative fFXCO₂ enhancements along the satellite track
 401 are largely consistent. Consequently, these findings highlight the effectiveness of the background line method for inferring satellite-
 402 observed background XCO₂. They also emphasize that the spatial scale of satellite data analysis is closely linked to the constraints
 403 imposed by local emission sources. Neglecting the latitudinal gradient of background XCO₂ may introduce biases in the estimation
 404 of fFXCO₂ and, consequently, in derived emission fluxes (Ye et al. 2020).



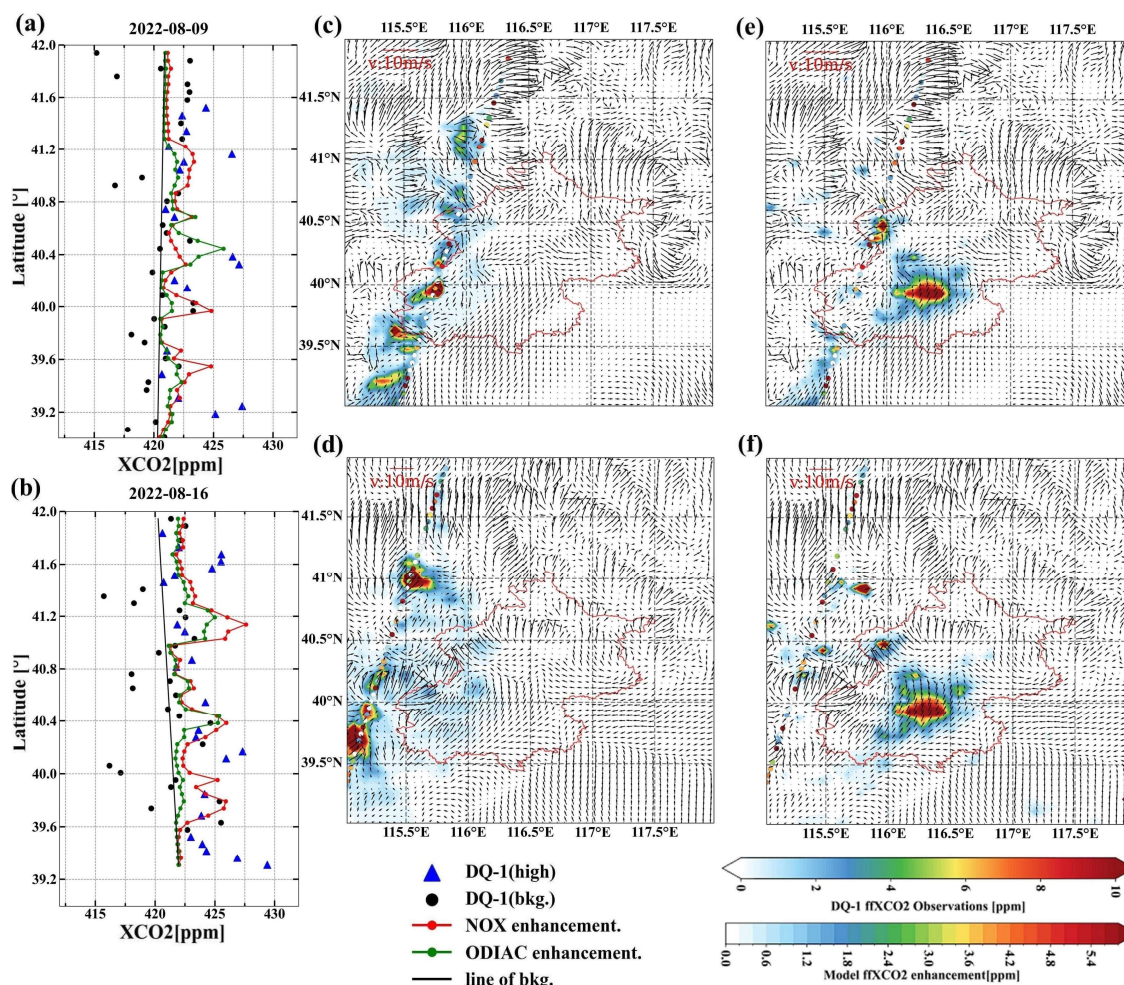
405
 406 **Figure 6** Similar to Fig. 5, comparison between simulated and observed fFXCO₂ enhancements using DQ-1 overpasses above Cairo on 2
 407 August 2022 at 11:00 UTC (panels a, c, e) and 19 August 2022 at 23:00 UTC (panels b, d, f). Panels (c) and (d) show the simulated fFXCO₂



408 enhancements based on the NO_x emissions, while panels (e) and (f) show those based on the ODIAC inventory.

409

410 **3.2.2. Comparison of NO_x and ODIAC Modeled ffXCO₂ in Beijing**



411

412 **Figure 7** Similar to Fig. 5, comparison between simulated and observed ffXCO₂ enhancements using DQ-1 overpasses above Beijing on 9
413 August 2022 at 18:00 UTC (panels a, c, e) and 16 August 2022 at 18:00 UTC (panels b, d, f). Panels (c) and (d) show the simulated ffXCO₂
414 enhancements based on the NO_x emissions, while panels (e) and (f) show those based on the ODIAC inventory.

415

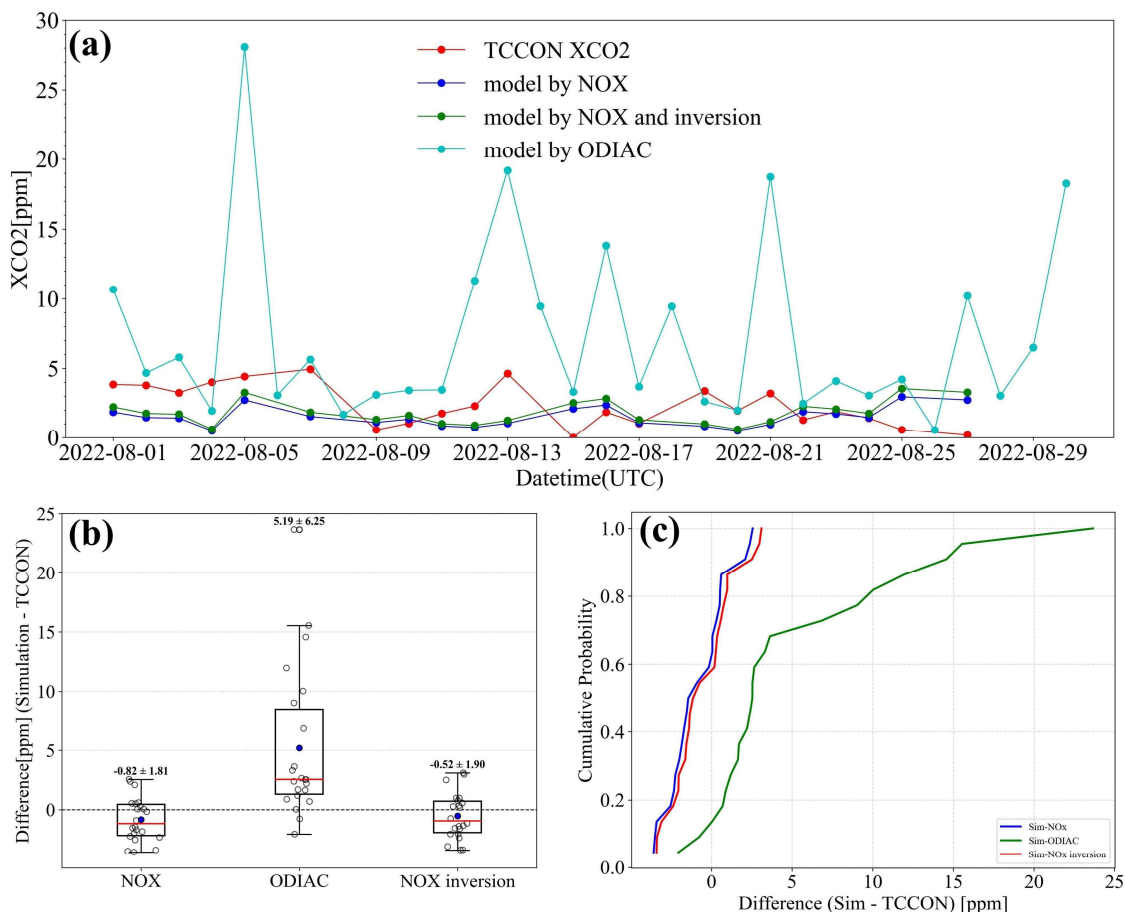
416 Figure 7 illustrates the investigation of local ffXCO₂ enhancements over Beijing using two DQ-1 overpasses and corresponding
417 simulated ffXCO₂. In the figure, the colored shading represents XCO₂ concentrations accumulated over the previous 24 hours
418 simulated by STILT, while the colored dots indicate satellite-observed XCO₂ enhancements, calculated by subtracting the



419 background values (see Section 2.2.2). The red contours outline the urban area of Beijing. As shown, ffXCO_2 over this region can
420 reach approximately 6.0 ppm.

421 Notably, simulations based on the NO_x inventory (Figs. 7c, d) show that the spatial distribution of ffXCO_2 enhancements varies
422 significantly with meteorological conditions and emission patterns. In contrast, for Paris and Cairo, the simulated ffXCO_2 is more
423 concentrated. Over Beijing, however, the ffXCO_2 distribution is more dispersed and comprises multiple plumes. When comparing
424 simulations using NO_x and ODIAC inventories for Paris and Cairo, the overall plume structures remain largely unaffected. Over
425 Beijing, the simulations using the ODIAC inventory (Figs. 7e, f) display an almost identical ffXCO_2 enhancement distribution across
426 different wind conditions, showing pronounced anomalies in the urban area. Such similarity is unrealistic.

427 We attribute this behavior to the ODIAC inventory allocating disproportionately high fossil fuel emissions to central Beijing.
428 When STILT footprints intersect the urban area, the high emission gradients in ODIAC (central urban emissions far exceeding
429 suburban values) amplify ffXCO_2 enhancements in the inner city. ODIAC's low-emission thresholds are influenced by nighttime
430 light saturation, with median differences ranging from 47% to 84%. Consequently, ODIAC artificially concentrates emissions in the
431 city center while underrepresenting surrounding suburban areas. This makes it challenging to accurately constrain CO_2 fluxes in the
432 peripheral regions using ODIAC. Observations from the TCCON Xianghe site further highlight the limitations of ODIAC's emission
433 allocation in the Beijing area.



434

435 **Figure 8** Comparison of ffXCO₂ observed at the TCCON Xianghe site in Beijing during August with ffXCO₂ simulated using the NO_x
 436 inventory and the ODIAC inventory. Panel (a) shows the ffXCO₂ observed by TCCON (red line), simulated ffXCO₂ using the NO_x
 437 emissions (dark blue line), simulated ffXCO₂ using the ODIAC inventory (light blue line), and simulated ffXCO₂ using the posterior NO_x
 438 emissions (green line). Panel (b) presents the distribution of differences between simulated ffXCO₂ (from the NO_x and ODIAC inventories)
 439 and TCCON observations throughout August, with bold numbers indicating the mean and standard deviation. Panel (c) shows the
 440 cumulative probability distributions of the differences between simulated ffXCO₂ (NO_x emissions and ODIAC inventory) and TCCON
 441 observations.

442

443 Figure 8 presents the comparison of August ffXCO₂ at the TCCON site with simulations using the ODIAC and NO_x inventories.
 444 Unlike the ffXCO₂ calculation described in Section 2.2.2, the TCCON observations provide daily-averaged fossil fuel CO₂
 445 enhancements, where TCCON ffXCO₂ is calculated as TCCON XCO₂ minus background XCO₂ and NEE contributions (details in
 446 the Appendix A3). In Figure 8a, the dark blue line represents ffXCO₂ simulated at the TCCON site using the NO_x inventory, the
 447 green line shows the ffXCO₂ simulated after optimization with the inversion using DQ-1 observations, the light blue line corresponds
 448 to ODIAC-based simulations, and the red line depicts TCCON-observed ffXCO₂.



449 Figure 8b quantifies the accuracy of the simulations by plotting the difference between the simulated ffXCO_2 and TCCON
 450 observations on the same day and summarizing the monthly mean and standard deviation. The monthly mean absolute difference
 451 for the NO_x inventory is 0.82 ppm, while ODIAC exhibits a much larger discrepancy of 5.19 ppm. The inversion-constrained NO_x
 452 inventory reduces the mean absolute difference to 0.52 ppm, closely matching TCCON observations. Figure 8c shows the
 453 cumulative probability distribution of the differences between simulated and observed ffXCO_2 . The differences for the NO_x and
 454 inversion-constrained NO_x simulations are largely centered around zero (blue and red lines), whereas for ODIAC, approximately
 455 30% of differences exceed 5 ppm.

456 These results indicate that for Beijing in August, simulations based on the NO_x inventory outperform those using ODIAC.
 457 Given that the prior ffCO_2 emissions in both inventories are of similar magnitude, the observed discrepancies are primarily
 458 attributable to the spatial allocation of emissions in ODIAC. The combined inversion using TROPOMI and ACDL data provides a
 459 more accurate reconstruction of urban ffXCO_2 plume structures.

460 3.2.3. ffCO_2 Inversion Results

461 **Table 2 Results of inversion of for CO_2 -to- NO_x ratio selected cities using DQ-1 XCO_2 data**

City	Overpass	Prior CO_2 -to- NO_x ratio (λ)	Prior uncertainty (%)	Observation uncertainty (ppm)	Model transport uncertainty (ppm)	Posterior CO_2 -to- NO_x ratio (λ) and uncertainty (%)
Cairo	2022/08/02	470	40.59%	1.23	1.75	428±64.58
	2022/08/19			1.06	2.10	512±96.56
Paris	2022/08/07	601	30.12%	2.45	0.36	731±107.60
	2022/08/21			1.68	0.76	742±138.53
Beijing	2022/08/09	694	28.12%	2.31	1.28	640±90.11
	2022/08/16			1.79	3.25	553±89.80

462 This section presents the inversion results of urban carbon emissions for Cairo, Paris, and Beijing, based on TROPOMI and
 463 DQ-1 satellite overpass observations (see Table 2). In the inversion, we systematically accounted for observational errors and
 464 uncertainties in atmospheric transport to improve the reliability of the emission estimates. From the posterior results, we derived
 465 city-specific CO_2 -to- NO_x ratios and, by combining them with TROPOMI-derived NO_x emissions, further quantified fossil fuel CO_2
 466 (ffCO_2) emissions. This approach not only enables quantitative assessment of emissions but also provides a scientific basis for cross-
 467 city comparisons of emission characteristics, while demonstrating the potential of multi-satellite data for urban emission monitoring.

468 For the selected orbits, the posterior CO_2 -to- NO_x ratios were 428–512 for Cairo, 731–742 for Paris, and 553–640 for Beijing



469 (Table 2). These ratios exhibited clear temporal variability under different background conditions. The magnitude of emissions
470 captured by each orbit depended strongly on its distance from major emission regions and the contemporaneous domain-averaged
471 wind conditions (Che et al. 2022). The domain-averaged wind speeds for the study month (Fig. 9), as well as the high-resolution
472 wind fields at overpass time (black arrows in Figs. 5–7), were consistently greater than 3 m s^{-1} . Under such meteorological conditions,
473 the posterior estimates represent emissions from several hours prior to satellite overpass. The posterior uncertainties of the CO_2 -to-
474 NO_x ratio were 15.09%–18.86% for Cairo, 14.72%–18.67% for Paris, and 14.08%–16.24% for Beijing. Overall, uncertainties were
475 larger for Cairo and Paris compared with Beijing.

476 As described in section 4.1, the prior uncertainty of the CO_2 -to- NO_x ratio was prescribed based on available statistics and
477 emission characteristics. Owing to more comprehensive statistics and advanced manufacturing processes, large metropolitan areas
478 typically exhibit better-characterized emission features. Accordingly, the prior uncertainties for Beijing and Paris were smaller than
479 those for Cairo. Table 2 further shows that the relative contributions of observational and transport errors differed across cities. In
480 Cairo, transport errors dominated over observational errors, whereas in Paris the opposite held true. For Beijing, the relative
481 magnitudes of transport and observational errors varied across orbits. The overall smaller posterior uncertainty for Beijing compared
482 to Cairo and Paris reflects its more stable prior emission characteristics.



483
 484 **Figure 9 Monthly mean wind rose plots for Cairo, Paris, and Beijing in August.**

485 **3.3. The Uncertainty of Transport Model**

486 Atmospheric transport modeling uncertainty has been recognized as a major factor affecting emission constraints(Wu et al.
 487 2018). Systematic errors arising from a combination of transport model biases and misrepresented statistical inputs can reduce the
 488 magnitude and spatial coverage of terrestrial uncertainty reductions by roughly a factor of two(Wang et al. 2014). Notably, transport-
 489 related uncertainties in ffXCO₂ represent a key source of error in inverse emission estimates(Ye et al. 2020). In this section, we
 490 quantify the impact of transport errors on simulated XCO₂ arising from uncertainties in horizontal wind fields and vertical mixing,
 491 with a focus on their influence on the inversion of ffXCO₂ fluxes.

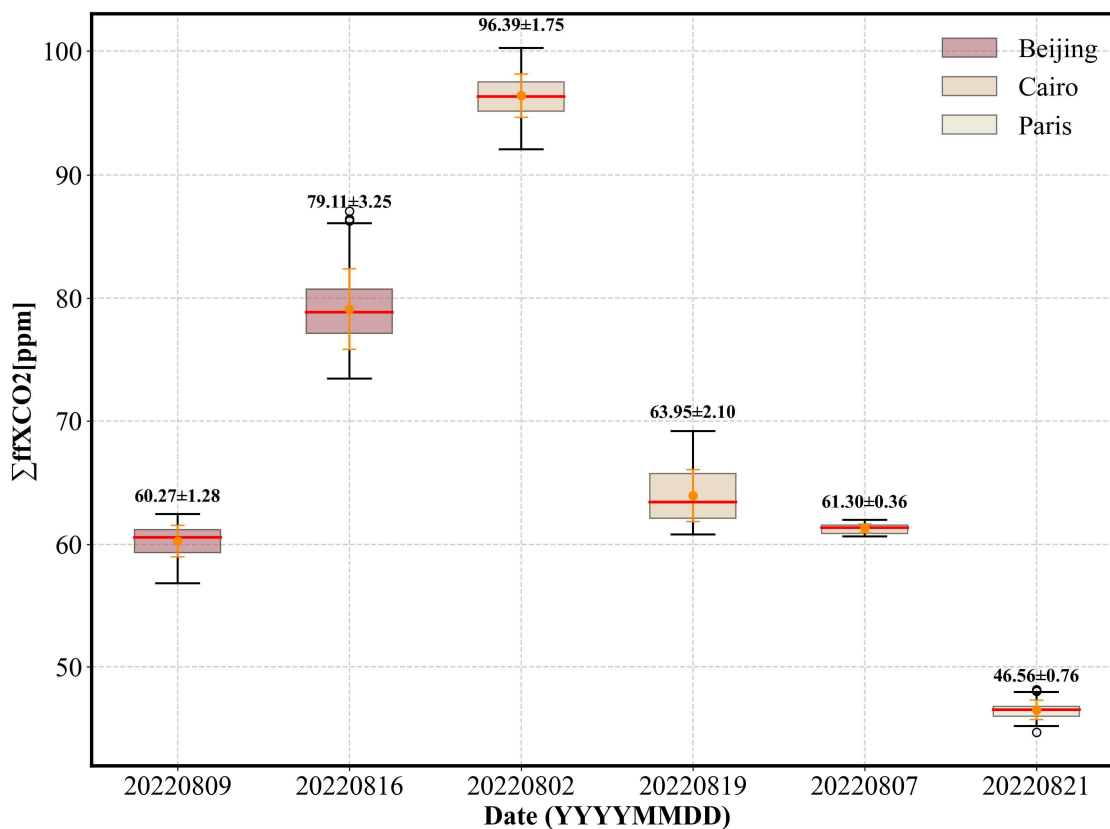
492 Errors induced by wind field uncertainties propagate through the model and affect the accuracy of CO₂ emission
 493 estimates(Sheng et al. 2025). Previous studies have accounted for column transport errors by weighting variance relative to pressure
 494 and treating each model level independently(Lin and Gerbig 2005; Wu et al. 2018). Ye et al. 2020 further quantified ffXCO₂



495 simulation uncertainty by introducing random perturbations in wind speed and direction. Building on these approaches, we
496 investigate how horizontal wind speed and wind direction errors influence inversion performance.

497 Here, horizontal transport error is propagated through the model via its effect on ffXCO_2 plume dispersion. For the selected
498 cities, errors are assumed to be unbiased. Wind direction uncertainty is represented by rotating the plume around the emission center,
499 followed by the addition of random wind speed perturbations to the rotated plume. Using DQ-1 wind field data, random errors were
500 added at each model level (wind direction perturbation between -10° and 10° , wind speed perturbation between -1 m/s and 1 m/s),
501 and the STILT footprints were recomputed to obtain plume-averaged footprints with random errors included (Yi et al. 2024).

502 In total, 10^4 simulations were conducted, with the ffXCO_2 integrated along each satellite track. The standard deviation (1σ) of
503 these simulations is used to represent the uncertainty in simulated ffXCO_2 resulting from horizontal transport errors (Figure 10).



504
505 **Figure 10** Boxplots of modeled integrated ffXCO_2 enhancements ffXCO_2 along selected DQ-1 overpasses for the three cities (distinguished
506 by box color) with dates labeled on the x-axis. For each box, the central line represents the median (q2), and the bottom and top edges
507 represent the 25th and 75th percentiles (q1 and q3), respectively. Whiskers extend to the minimum and maximum values. Numbers
508 indicate the mean \pm standard deviation.

509

510 Figure 10 presents the total simulated ffXCO_2 along DQ-1 overpasses for the different study regions. Overall, the simulated



511 ffXCO₂ totals for the three cities are of comparable magnitude. Notably, compared with Beijing and Cairo, the horizontal transport
512 uncertainty along the two Parisian tracks is the lowest, at 0.36 ppm and 0.76 ppm, respectively. In Cairo, the satellite tracks traverse
513 the edges of emission plumes, making the simulations highly sensitive to wind speed and direction, which results in larger transport
514 model errors. Beijing, with its complex terrain and variable wind fields, exhibits more intricate transport uncertainties relative to
515 the other two cities. These observations indicate that transport model uncertainty is closely related to city-scale emissions, the
516 relative alignment of plumes and satellite tracks, model performance, and local topography. Variations in these factors contribute to
517 temporal changes in posterior emission uncertainties along different tracks.

518 Vertical turbulent mixing governs the vertical transport of air parcels and controls the dilution of surface emissions within the
519 boundary layer (Vertical mixing in atmospheric tracer transport models: error characterization and propagation). Although column-
520 integrated measurements may be less sensitive to the vertical distribution of tracers than in situ observations, errors in planetary
521 boundary layer (PBL) height can still affect column simulations due to wind shear and its interaction with vertical redistribution of
522 tracers (Planetary boundary layer errors in mesoscale inversions of column-integrated CO₂ measurements). It is worth noting that
523 the ACDL instrument includes an aerosol channel capable of providing extinction coefficient profiles and planetary boundary layer
524 height (PBLH) products(Dai et al. 2024). In this study, PBLH data derived from ACDL retrievals are used in the simulations, helping
525 to mitigate errors arising from inaccurate boundary layer height assumptions. Therefore, boundary layer height errors are not
526 considered in the estimation of ffXCO₂.

527 **4. Importance of Satellite Observations for Optimizing the CO₂-to-NO_x Ratio**

528 **4.1. Variations in CO₂-to-NO_x ratio calculation methods**

529 Recently, an increasing number of studies have employed NO_x emissions to estimate ffCO₂ emissions(Berezin et al. 2013; Feng
530 et al. 2024; Xu et al. 2025; Yang et al. 2023; Zhang et al. 2022; Zheng et al. 2020). In inversion methods based on NO_x emissions,
531 the choice of the prior CO₂-to-NO_x ratio directly affects the emission estimates. Uncertainty in the prior ratio propagates to the
532 estimated ffCO₂ emissions, influencing both their magnitude and spatial distribution. To evaluate this effect, we selected several
533 widely used CO₂-to-NO_x ratio calculation methods and systematically assessed their associated uncertainties (results see Appendix
534 A6).

535 - M.1 Grid-level CO₂-to-NO_x ratio derived directly from gridded CO₂ and NO_x inventories(Feng et al. 2024). Since this study
536 scales emissions to the city level, we further fitted the grid-level ratios to obtain city-integrated CO₂-to-NO_x ratios. M.1
537 calculations were based on the GEMS gridded inventory.

538 - M.2 CO₂-to-NO_x ratios calculated using sectoral emission factors for CO₂ and NO_x(Zheng et al. 2020). We derived city-scale
539 ratios by aggregating across all sectors. M.2 used the GEMS sectoral inventory.



540 - M.3 CO₂-to-NO_x ratios derived from near-real-time satellite observations. Background-stable NO_x plumes were used to
541 constrain CO₂ plumes, and joint fitting of the two concentrations was performed using the cross-sectional flux method(Reuter
542 et al. 2019; Xu et al. 2025). The CO₂-to-NO_x ratio was obtained directly from the half-width at half-maximum. Following this
543 approach, we used TROPOMI and OCO-2 observations to calculate city-scale ratios.

544 - M.4 Same as M.2, but the MEIC sectoral inventory was used for Beijing.

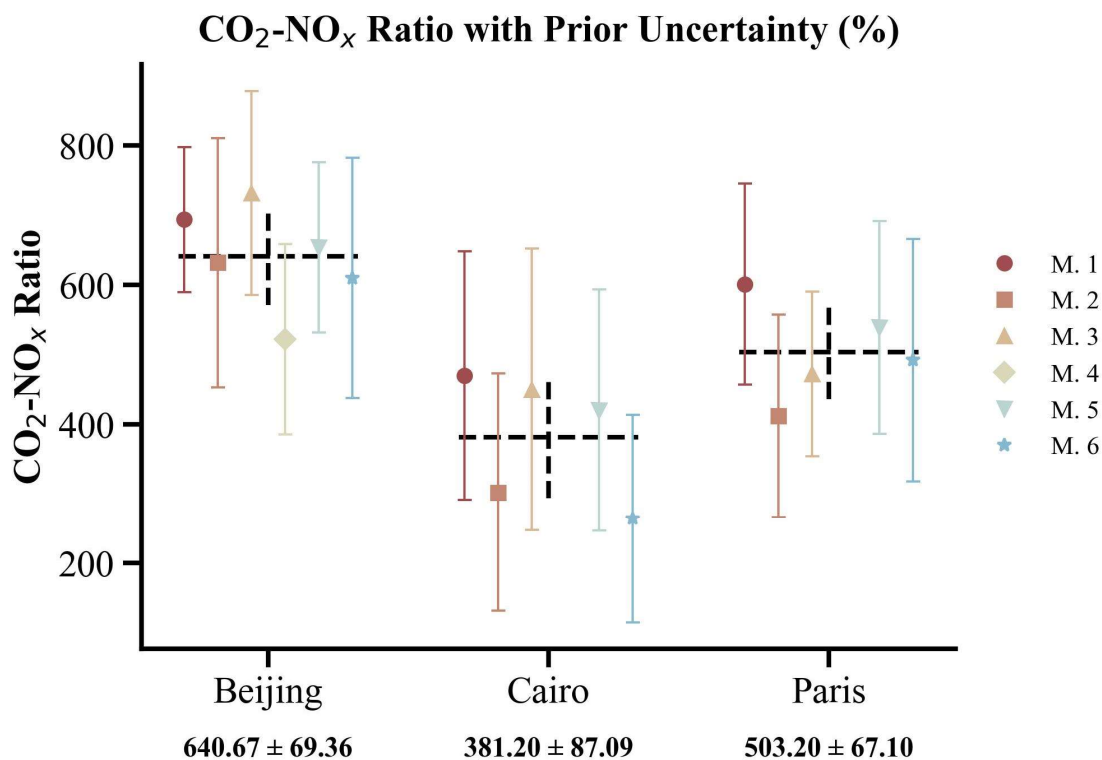
545 - M.5 Same as M.1, but calculations were based on the EDGAR gridded inventory.

546 - M.6 Same as M.2, but calculations were based on the EDGAR sectoral inventory.

547 We systematically accounted for the uncertainties associated with the prior CO₂-to-NO_x ratios for each method. The uncertainty
548 of the CO₂-to-NO_x ratio arises from the uncertainties of the underlying emissions. For Method 1, a Monte Carlo simulation was
549 performed: CO₂ and NO_x inventory uncertainties (Huang et al. 2017; Wang et al. 2013) were used to generate random perturbations
550 at each grid, and the CO₂-to-NO_x ratio was recalculated 10,000 times to obtain the distribution characteristics. The prior CO₂-to-
551 NO_x ratio uncertainty was expressed as R90/M, where R90 is the range between the 95th and 5th percentiles and M is the median
552 value from 10,000 Monte Carlo simulations. For Method 2, the uncertainty was represented as:

553
$$\sigma_{C/N} = \sqrt{\sigma_{NO_x}^2 + \sigma_{FFCO_2}^2} \quad (14)$$

554 where σ_{NO_x} and σ_{FFCO_2} denote the uncertainties of the NO_x and ffCO₂ emission factors, respectively. Notably, for each
555 method, the use of different inventories requires adjustment of the assigned uncertainties (see Appendix A6). In Method 3, the prior
556 CO₂-to-NO_x ratio uncertainty was derived from the quadratic sum of observational uncertainties in NO₂ and CO₂ concentrations and
557 the Gaussian fitting uncertainty.



558

559 **Figure 11** Results of CO₂-to-NO_x ratios obtained using different calculation methods for Beijing, Cairo, and Paris. Different CO₂-to-NO_x
560 ratios within the same city are distinguished by color. Additionally, the mean and standard deviation of the different ratios for each city
561 are also shown.

562

563 In this section, we used six different CO₂-to-NO_x ratio calculation methods to estimate the city-scale ratios for Beijing, Cairo,
564 and Paris in August. Since the MEIC inventory is only available for Beijing, six prior CO₂-to-NO_x ratios were obtained for Beijing,
565 while five ratios were derived for Paris and Cairo. Figure 11 presents the CO₂-to-NO_x ratios and their associated uncertainties for
566 each city using the different methods. We also calculated the mean and standard deviation of the ratios across methods, reflecting
567 both the overall understanding of the city-scale prior CO₂-to-NO_x ratio and the variability arising from methodological
568 differences.

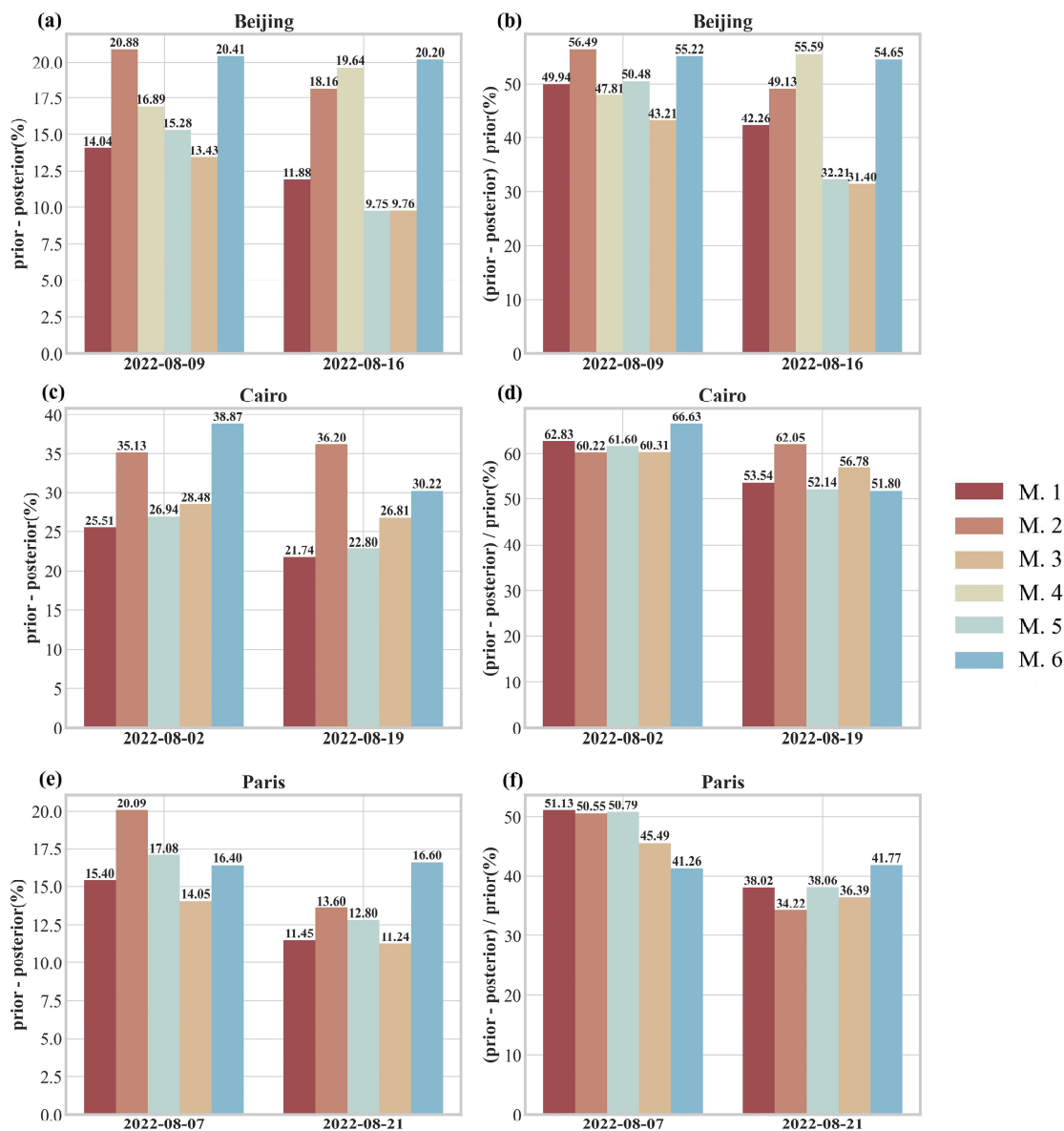
569 The results consistently show the ordering Beijing > Paris > Cairo. Moreover, more developed cities typically have better
570 production technologies and more detailed emission statistics (Oda et al. 2019; Ye et al. 2020). Consequently, the prior uncertainties
571 for Beijing and Paris are notably smaller than those for Cairo, and the variability of CO₂-to-NO_x ratios across methods is also reduced
572 for these cities.



573 **4.2. Bayesian Inversion for Reducing CO₂-to-NO_x Ratio Uncertainty**

574 Using different prior CO₂-to-NO_x ratios, we conducted the Bayesian inversion described in Section 2.2.2 to optimize the August
575 CO₂-to-NO_x ratios for Beijing, Cairo, and Paris along the respective DQ-1 satellite overpasses. Figure 12 shows the absolute
576 reduction in posterior uncertainty (posterior minus prior) and the relative reduction (prior minus posterior, divided by prior) for each
577 city across different orbits. For Beijing, the posterior uncertainty decreased by 9.75%–20.88%, corresponding to a 31.4%–56.49%
578 reduction relative to the prior. In Cairo, the posterior uncertainty decreased by 21.74%–38.87%, equivalent to a 51.8%–66.63%
579 reduction, while in Paris the reduction ranged from 11.24% to 20.09%, corresponding to a 34.22%–51.13% decrease relative to the
580 prior.

581 These results indicate that, for all cities, the posterior uncertainties were significantly reduced regardless of the method used to
582 calculate the prior ratio. This demonstrates that constraining the inversion with DQ-1 ACDL observations substantially improves
583 the accuracy of ffCO₂ estimates derived from NO_x emissions. Notably, in Cairo—the city with the largest prior uncertainty—the
584 reduction in uncertainty after constraining with both active and passive satellite observations was the greatest, highlighting the
585 effectiveness of satellite data in mitigating emission uncertainties in cities with incomplete statistical information. These findings
586 underscore the potential of satellite remote sensing to supplement emission inventories and enhance the reliability of urban emission
587 estimates.



588

589 **Figure 12 Comparison of Bayesian inversion prior and posterior uncertainties for each orbit over different cities. Panels (a), (c), and (e)**
 590 **show the absolute reduction in uncertainty (prior uncertainty minus posterior uncertainty), while panels (b), (d), and (f) show the relative**
 591 **reduction in uncertainty (prior minus posterior uncertainty divided by prior uncertainty). Results from different prior CO₂-to-NO_x ratios**
 592 **are represented by bars in different colors, with the values displayed at the top of each bar.**

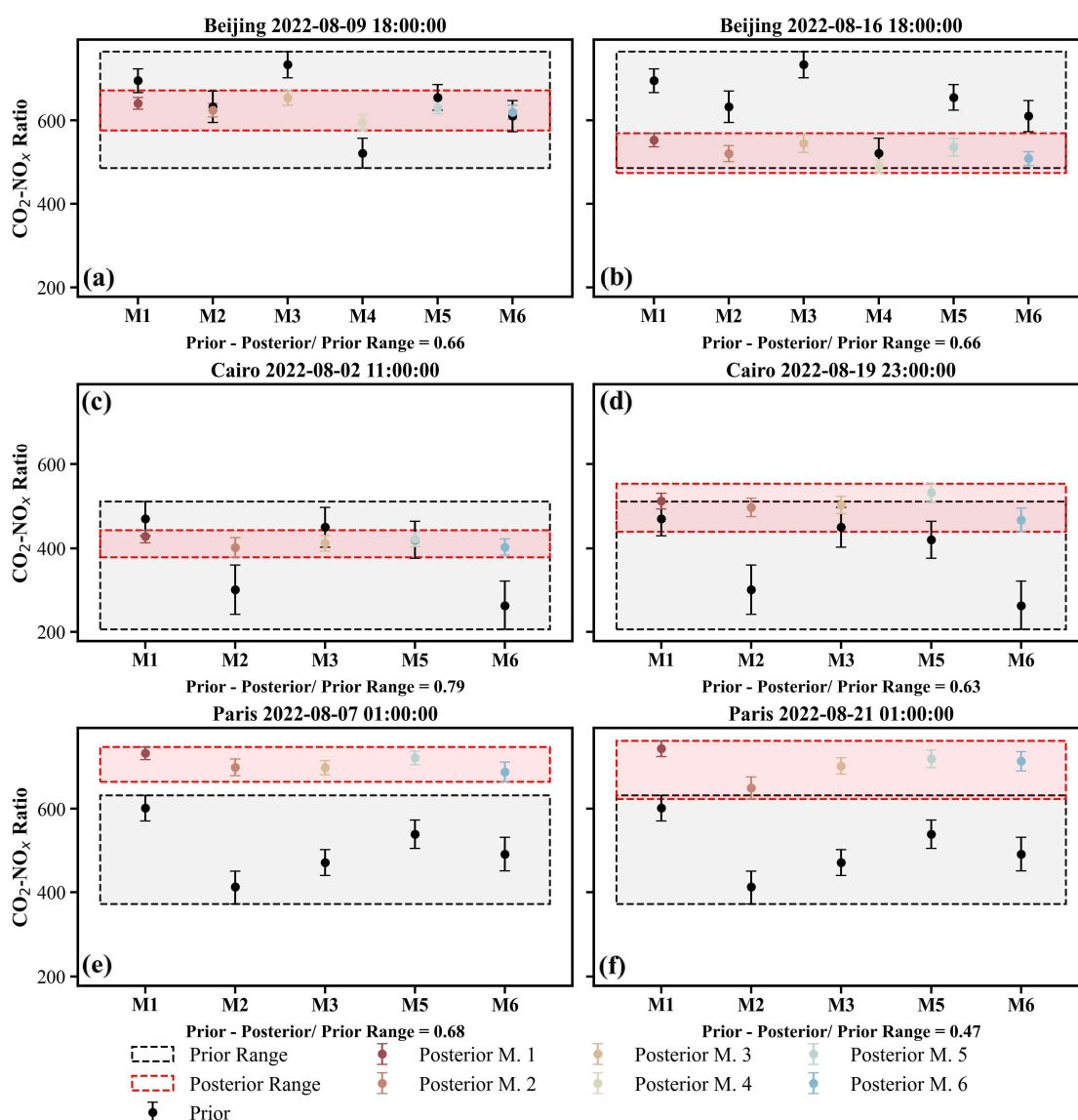
593

594 Furthermore, we examined the range of CO₂-to-NO_x ratios calculated for each city using different methods (Fig. 13). In the
 595 figure, the black boxes represent the prior distribution ranges, while the red boxes indicate the posterior distribution ranges. The
 596 distribution ranges illustrate the variability among CO₂-to-NO_x ratios obtained from different methods, and we also quantified the



597 reduction of the posterior range relative to the prior. Except for the orbit over Paris on 21 August, all other results show that the
 598 posterior ranges were reduced by more than 60% compared to the priors.

599 These results demonstrate that our approach effectively reduces the discrepancies arising from different CO₂-to-NO_x ratio
 600 calculation methods. That is, prior ratios derived from various methods are constrained to approximately the same range after
 601 inversion. This finding underscores the importance of using observational constraints to obtain more accurate CO₂-to-NO_x ratios in
 602 future ffCO₂ emission estimations.



603
 604 **Figure 13** Distribution ranges of prior and posterior CO₂-to-NO_x ratios calculated using different methods. Black boxes represent the
 605 range of prior CO₂-to-NO_x ratios, with posterior ratios indicated by black circles. Red boxes represent the range of posterior CO₂-NO_x



606 ratios, with posterior uncertainties from different methods shown using different colors and symbols.

607 5. Summary

608 Accurate identification and quantification of anthropogenic CO₂ emissions form a critical scientific basis for national emission
609 reduction policies and carbon sink strategies. However, bottom-up inventory approaches typically operate on long compilation
610 cycles (e.g., annual), making it difficult to capture short-term or near-real-time emission dynamics. Most inventories provide only
611 annual totals and lack the temporal resolution needed to characterize daily, hourly, or event-driven emissions.

612 In this study, we developed a city-scale ffCO₂ inversion framework that integrates both active and passive satellite observations
613 of greenhouse gases. This framework enables high-resolution estimation of fossil fuel emissions at satellite overpass times and over
614 preceding hours, while simultaneously constraining the city-scale CO₂-to-NO_x ratio. A key feature of the approach is its reduced
615 reliance on prior emission inventories, allowing rapid and objective identification and quantification of anthropogenic emission
616 signals at regional scales, thereby enhancing the monitoring and verification of urban emission dynamics. In this framework,
617 satellite-observed XCO₂ enhancements attributed to urban emissions are used to constrain WRF-STILT atmospheric transport
618 simulations of anthropogenic CO₂. This process not only enables quantitative assessment of urban fossil fuel emissions but also
619 provides independent evidence for improving emission inventories and refining urban carbon accounting systems. The study
620 highlights the potential of combining multi-source satellite observations with transport models and lays a foundation for future city-
621 scale ffCO₂ inversions based on the CO₂-to-NO_x ratio. Furthermore, we discuss the impact of the lack of standardized CO₂-to-NO_x
622 ratio calculation methods on urban emission estimates and demonstrate that observational constraints on city-scale ratios can
623 substantially improve ffCO₂ estimation from a carbon-nitrogen co-optimization perspective. Using a Bayesian inversion approach,
624 we optimized the CO₂-to-NO_x ratios for Cairo, Paris, and Beijing in August 2022 based on DQ-1 satellite overpasses and estimated
625 the cities' fossil fuel CO₂ emissions using TROPOMI NO₂ data. The resulting CO₂-to-NO_x ratios ranged from 428–512, 731–742,
626 and 553–640 for Cairo, Paris, and Beijing, respectively, indicating significant day-to-day variability in emission estimates. Cairo
627 exhibited the largest posterior uncertainty, primarily due to high prior uncertainty and transport model errors. Differences in posterior
628 uncertainties across orbits were also closely related to meteorological conditions and the relative position of the satellite tracks to
629 urban plumes. We further compared ffXCO₂ enhancement distributions simulated using the ODIAC inventory. Results for Cairo
630 and Paris were broadly consistent with TROPOMI-based simulations, while notable differences emerged for Beijing. TCCON XCO₂
631 observations were used to interpret these discrepancies. The monthly mean ffXCO₂ enhancement derived from TROPOMI NO₂ data
632 differed from TCCON measurements by less than 1 ppm, whereas the ODIAC-based results deviated by 5.16 ppm. This highlights
633 the need to account for uncertainties arising from inventory allocation and outdated updates when interpreting XCO₂ inversion
634 results. We systematically examined the impact of different prior CO₂-to-NO_x ratio calculation methods on urban ffCO₂ inversions.
635 In our study, methodological differences led to variations of 10.8%–22.8% in prior ratios. Importantly, regardless of the prior ratio



636 or its uncertainty, DQ-1 observations constrained the posterior values to a similar range, substantially reducing discrepancies among
637 different calculation methods.

638 Looking ahead, improving satellite-based city-scale ffCO_2 inversions will require accounting for the spatiotemporal
639 correlations of prior emission errors. Our current framework does not yet incorporate this aspect, which imposes certain limitations
640 on the interpretation and application of the results. Satellite observations are inherently constrained by inversion errors, sampling
641 geometry, and revisit frequency, limiting overpass opportunities. A single prior factor, such as a uniform CO_2 -to- NO_x ratio, cannot
642 fully capture the complex spatiotemporal features of emissions. Incorporating prior error correlations can mitigate uncertainties
643 arising from sparse observations and better resolve temporal and spatial variability in urban emissions. Moreover, the number of
644 satellite tracks required to constrain city emissions depends on the desired emission resolution and uncertainty thresholds relevant
645 for policy applications. Lower temporal resolution may suffice for long-term trend analysis, whereas capturing short-term peaks or
646 episodic emissions necessitates higher observation frequency and precision. This consideration aligns with emerging international
647 approaches emphasizing multi-platform, multi-temporal observations, combining polar-orbiting, geostationary satellites, and
648 ground-based monitoring to achieve multidimensional constraints on urban emissions.

649 Overall, our results demonstrate that coupling high-resolution atmospheric transport simulations with a Bayesian inversion
650 framework allows TROPOMI and DQ-1 multi-source observations to effectively constrain urban ffXCO_2 enhancement signals. The
651 approach captures spatial heterogeneity of emissions, particularly in cities with strong emission intensities and well-defined plume
652 structures, providing a robust basis for quantitative analysis. Furthermore, current methods estimating ffCO_2 from NO_x emissions
653 often lack explicit treatment of CO_2 -to- NO_x ratio uncertainty, which can significantly influence inversion outcomes. Differences
654 among calculation methods for the same region can be as large as 258–304. Notably, our inversion framework substantially reduces
655 CO_2 -to- NO_x ratio uncertainty, providing more stable priors for urban ffCO_2 estimation. Recent studies suggest the need to further
656 optimize CO_2 -to- NO_x emission ratios at regional scales to improve ffCO_2 estimates (Feng et al. 2024). Therefore, we recommend
657 that future NO_x -based ffCO_2 inversion studies adopt observational constraints to refine CO_2 -to- NO_x ratios, minimizing errors arising
658 from prior ratio uncertainties.

659 Appendix

660 A1: ACDL XCO_2 Data Inversion

661 Unlike passive satellite XCO_2 products (e.g., OCO-2/3), the DQ-1 XCO_2 product—hereafter referred to as $\text{XCO}_2^{\text{Lidar}}$ to
662 distinguish it from passive measurements—is derived from the differential absorption between ACDL’s on-band wavelength (strong
663 CO_2 absorption) and off-band wavelength (weak CO_2 absorption). Here, “WF(p)” refers to the lidar signal and integrated weighting
664 function introduced in Section 2.1.1, with “p” representing atmospheric pressure:



665
$$XCO_2^{Lidar} = \frac{2 \cdot \ln\left(\frac{V_{off} \cdot V_{on-0}}{V_{on} \cdot V_{off-0}}\right)}{\int_{p_{surface}}^{p_{toa}} WF(p) dp} \quad (A1)$$

666 Here, V_{on} and V_{off} denote the reflected signal energies at the on-band and off-band wavelengths, respectively, while V_{on-0}
 667 and V_{off-0} correspond to the transmitted signal energies. $p_{surface}$ represents the atmospheric pressure at the sub-satellite point
 668 of the laser, and p_{toa} denotes the pressure at the top of the atmosphere. The denominator in Equation A1 represents the integrated
 669 weighting function ($WF(p)$), which can be expressed according to (Refaat et al. 2016) as:

670
$$WF(p) = \Delta\sigma_{wf}(\lambda_{on}, \lambda_{off}, p) \cdot N_{dry}(p) \quad (A2)$$

671 Here, $\Delta\sigma_{wf}(\lambda_{on}, \lambda_{off}, p)$ represents the differential absorption cross-section of CO_2 between the on-band λ_{on} and off-band λ_{off}
 672 wavelengths at pressure p . N_{dry} denotes the number of dry air molecules per unit area within the corresponding pressure layer.

673

674 **Table A1 DQ-1 ACDL operating parameters**

Parameters	Values
Orbit altitude	705km
Lidar footprint diameter	~70m
Horizontal spacing of lidar footprints	~350m
Field of view	<0.2mrad
Telescope diameter	1000nm
Divergence angle after laser beam expansion	<0.1mrad
Repetition frequency	20Hz
Laser pulse width	<50ns
Laser energy	75mJ
Off-line wavelength	1572.085nm
On-line wavelength	1572.024nm

675

676 **A2: Derivation of the Principle of Mass Balance**

677 For satellite column observations of specific species such as NO_2 , the mass balance equation can be expressed as follows:



678

$$\begin{cases} \frac{\partial V_{NO_2}}{\partial t} + \nabla \cdot \vec{F}_{NO_2} = E_{NO_2} - S \\ \vec{F}_{NO_2} = V_{NO_2} \vec{u}_{100} \\ S \approx \frac{V_{NO_2}}{\tau} \end{cases} \quad (A3)$$

679 Here, V_{NO_2} represents the columnar NO_2 concentration observed by TROPOMI, defined as a scalar function of x and $\nabla =$
 680 $\left(\frac{\partial}{\partial x}, \frac{\partial}{\partial y}\right)$ denotes the gradient operator; $\vec{F}_{NO_2} = (F_x, F_y)^T$ is the horizontal flux, with units of $\text{mol} \cdot \text{m}^{-2} \cdot \text{s}^{-1}$, expressed as a vector
 681 function of x and y and weighted by the wind vector. The 100 m wind field is commonly used to characterize horizontal transport
 682 within the planetary boundary layer (PBL)(Sun 2022). τ represents the first-order chemical lifetime of NO_2 in seconds.

683 By solving the system of equations in Equation A3 and expanding the horizontal flux divergence using vector calculus, we
 684 obtain the derivation of Equation A4 from Equation A3:

685

$$\begin{cases} \vec{u}_{100} \cdot (\nabla V_{NO_2}) + V_{NO_2} (\nabla \cdot \vec{u}_{100}) = \nabla \cdot \vec{F}_{NO_2} \\ E_{NO_2} = \frac{\partial V_{NO_2}}{\partial t} + \nabla \cdot \vec{F}_{NO_2} + \frac{V_{NO_2}}{\tau} \end{cases} \quad (A4)$$

686 Sun et al. 2022, in their first-principles derivation, introduced a "topographic correction term" to replace the wind divergence
 687 term $V_{NO_2} (\nabla \cdot \vec{u}_{100})$. Beirle et al. 2023 demonstrated that incorporating a topographic correction significantly improves the inversion
 688 of power-plant NO_x emissions based on the divergence method. Koene et al. 2024 carefully compared these two terms in the
 689 derivation of the divergence method, showing that they originate from the continuity equations of the source and non-source terms,
 690 and that numerically, the wind divergence and wind-topography terms are approximately equal in the absence of observational
 691 errors.

692 Despite their numerical equivalence in derivation, the accuracy of reanalyzed wind fields is generally lower than that of surface
 693 elevation data. Therefore, in practical measurements—particularly in complex, fine-scale settings—the wind divergence term alone
 694 may not provide sufficient constraint. Correcting wind divergence artifacts using topographic gradients is more feasible, especially
 695 in regions with rugged terrain. Accordingly, we revise Equation A5 using Equation A4 as follows:

696

$$\frac{V_{NO_2} \vec{u}_{10} \cdot (\nabla z_0)}{H} \approx V_{NO_2} (\nabla \cdot \vec{u}_{100}) \quad (A5)$$

697 Here, $\frac{V_{NO_2} \vec{u}_{10} \cdot (\nabla z_0)}{H}$ represents the topographic correction term, where the 10 m wind is approximated as the near-surface wind,
 698 and H denotes the gas scale height in meters. Following previous studies (Beirle et al. 2023; Liu et al. 2021; Sun 2022), Equation
 699 A5 is assimilated over both temporal and spatial dimensions. This procedure is concisely represented using the operator $\langle f \rangle$, as
 700 introduced in the derivations by Liu et al. and Sun et al. Ultimately, this approach allows the derivation of the vertical NO_2 flux on
 701 a grid-resolved basis.



702 **A3: Atmospheric Model Setting**

703 In this study's application of STILT, hourly outputs from version 4.0 of WRF are used to provide high resolution meteorological
704 fields, with the model grid configured to 32 vertical (eta) layers. The 6-hourly NCEP FNL (Final) global operational analysis data
705 ($\Delta t = 0.25^\circ$, $0.25^\circ \times 0.25^\circ$) are used as initial and boundary conditions for meteorological and land surface fields to provide the
706 initial and boundary conditions for WRF runs. The simulations run for 30 hours, but only the 7th to 30th hours of each simulation
707 are used to avoid spin-up effects in the first 6 hours.

708 In this study, we used the STILT model, version 2, to simulate atmospheric transport processes. STILT is configured to release
709 500 particles per receptor each time, with forward dispersion over 24 hours. The particle release heights for STILT are set within
710 the range of 50-1000 m, with releases every 50 m, and 1000-2000 m, with releases every 100 m, the spatial resolution of the STILT
711 simulations is $1 \text{ km} \times 1 \text{ km}$. Generally, as MAXAGL increases from 1 km to 2 km, the urban enhancement increases and then
712 stabilizes.

713 **Table A2 Model version information used in this study**

Model	Version
STILT(Stochastic Time-Inverted Lagrangian Transport)	V2
WRF(Weather Research and Forecasting)	V4.0
X-STILT(X-Stochastic Time-Inverted Lagrangian Transport model)	V1

714

715 **A4: Calculation of NEE XCO₂ enhancement**

716 We performed vertical integration following the method provided by the TCCON team, using the 51 altitude levels listed in
717 the publicly available ak_altitude dataset, which also serve as input heights for the STILT model. In contrast to the XSTILT
718 calculation method used for DQ-1, we applied the integration operator integration_operator_x2019 together with the mean averaging
719 kernel ak_xco2 to the STILT footprints across the 51 levels in order to generate the simulated XSTILT values required for this study.
720 We selected the National Institute for Environmental Studies (Japan) data-driven Upscale Product of Global Gross Primary
721 Production (NEE) as the reference for the overall local NEE during the DQ-1 overpasses. By convolving the NEE inventory with
722 XSTILT, we simulated the XCO₂ enhancement at TCCON sites attributable to NEE.

723 **A5: Calculation of Priori NO_x Emission Uncertainty**

724 The uncertainty of the NO_x inventory derived from the mass balance approach can be estimated using the error propagation
725 law as follows:



726
$$\varepsilon_{NOx} = \sqrt{\varepsilon_{\alpha}^2 + \varepsilon_{NO_2}^2}$$
 (A6)

727 where ε_{α} represents the uncertainty in the NO_x/NO_2 ratio, and ε_{NO_2} denotes the uncertainty in the NO_2 flux field. The latter
 728 can be further decomposed as:

729
$$\varepsilon_{NO_2} = \sqrt{\varepsilon_{TROPOMI}^2 + \varepsilon_{Wind}^2 + \varepsilon_{Fit}^2}$$
 (A7)

730 Here, $\varepsilon_{TROPOMI}$ is the uncertainty of the NO_2 column concentration, ε_{Wind} represents the uncertainty associated with the wind
 731 field, and ε_{Fit} accounts for the uncertainty in the fitted vertical scale height and chemical lifetime. The NO_2 uncertainty is calculated
 732 as the ratio of the standard deviation to the mean of the column concentrations within the study region and integrated over the time
 733 series. Wind field uncertainty is quantified through 10^4 Monte Carlo perturbations of wind speed and direction, with the propagated
 734 standard deviation representing the flux variability. The fitting uncertainty is obtained by performing 10^4 Monte Carlo draws of the
 735 grids involved in the fit, generating ensembles of scale heights and chemical lifetimes, with the final fitting error defined as the root
 736 mean square of the standard deviations of these ensembles.

737 **A6: Optimization results of the CO₂-to-NO_x ratio obtained using different calculation methods**

738 **Table A3 Inversion results of CO₂-to-NO_x ratios calculated using different methods**

Method	City	Date	Prior			Prior uncertainty (%)	Posterior CO ₂ -to-NO _x ratio (λ)	Posterior uncertainty (%)
			CO ₂ -to-NO _x ratio (λ)	CO ₂ -to-NO _x ratio uncertainty (%)	NO _x emission uncertainty (%)			
1	Beijing	2022/8/9	694	15	23.79	28.12	640	14.08
	Beijing	2022/8/16	694	15	23.79	28.12	553	16.24
	Cairo	2022/8/2	470	37.99	14.31	40.60	428	15.09
	Cairo	2022/8/19	470	37.99	14.31	40.60	512	18.86
	Paris	2022/8/7	601	24.04	18.15	30.12	731	14.72
	Paris	2022/8/21	601	24.04	18.15	30.12	742	18.67
2	Beijing	2022/8/9	632	28.28	23.79	36.96	624	16.08
	Beijing	2022/8/16	632	28.28	23.79	36.96	521	18.8
	Cairo	2022/8/2	302	56.56	14.31	58.34	402	23.21



	Cairo	2022/8/19	302	56.56	14.31	58.34	497	22.14
	Paris	2022/8/7	412	35.35	18.15	39.74	698	19.65
	Paris	2022/8/21	412	35.35	18.15	39.74	649	26.14
3	Beijing	2022/8/9	732	20.02	23.79	31.09	653	17.65
	Beijing	2022/8/16	732	20.02	23.79	31.09	545	21.32
	Cairo	2022/8/2	450	45.81	14.31	47.99	412	18.74
	Cairo	2022/8/19	450	45.08	14.31	47.99	503	20.41
	Paris	2022/8/7	472	24.83	18.15	30.75	697	16.84
	Paris	2022/8/21	472	24.83	18.15	30.75	701	19.65
	Beijing	2022/8/9	522	26.12	23.79	35.33	594	18.44
	Beijing	2022/8/16	522	26.12	23.79	35.33	491	15.69
5	Beijing	2022/8/9	654	18.72	23.79	30.27	630	14.99
	Beijing	2022/8/16	654	18.72	23.79	30.27	536	20.52
	Cairo	2022/8/2	420	41.32	14.31	43.73	421	16.79
	Cairo	2022/8/19	420	41.32	14.31	43.73	532	20.93
	Paris	2022/8/7	539	28.31	18.15	33.63	720	16.55
	Paris	2022/8/21	539	28.31	18.15	33.63	718	20.83
	Beijing	2022/8/9	610	28.28	23.79	36.96	619	16.55
	Beijing	2022/8/16	610	28.28	23.79	36.96	509	16.76
6	Cairo	2022/8/2	264	56.56	14.31	58.34	403	19.47
	Cairo	2022/8/19	264	56.56	14.31	58.34	467	28.12
	Paris	2022/8/7	492	35.35	18.15	39.74	687	23.34
	Paris	2022/8/21	492	35.35	18.15	39.74	712	23.14

739

740 **Declaration of Competing Interest**

741 The authors declare that they have no known competing financial interests or personal relationships that could have appeared
 742 to influence the work reported in this paper.



743 **Acknowledgments**

744 The authors thank all the financial support for this research. This research was supported by the National Key R&D Program
745 of China (Grant No. 2024YFB3910203), National Natural Science Foundation of China(Grant No. 42475144), the Fundamental
746 Research Funds for the Central Universities(2042025kf0036) and Beijing Natural Science Foundation (Grant No. L211045).

747 **Author contributions**

748 The experiment design was made by GH and JY. The data collection was done by JY, YH, HL, GH. JY completed the design
749 of the overall WRF-STILT model workflow, data collection, and result analysis. The data analysis was done by HZ, YZ, TS. WG
750 and SL provide funding. The paper was written by JY and GH. All authors have reviewed, commented on, and approved the paper.

751 **Reference**

- 752 Agency, I.E. (2009). World energy outlook. OECD/IEA Paris
- 753 Andres, R.J., Boden, T.A., Bréon, F.-M., Ciais, P., Davis, S., Erickson, D., Gregg, J.S., Jacobson, A., Marland, G., & Miller, J. (2012).
754 A synthesis of carbon dioxide emissions from fossil-fuel combustion. *Biogeosciences*, 9, 1845-1871
- 755 Beirle, S., Borger, C., Jost, A., & Wagner, T. (2023). Improved catalog of NO_x point source emissions (version 2). *Earth system
756 science data discussions*, 2023, 1-37
- 757 Berezin, E., Kononov, I., Ciais, P., Richter, A., Tao, S., Janssens-Maenhout, G., Beekmann, M., & Schulze, E.-D. (2013).
758 Multiannual changes of CO₂ emissions in China: indirect estimates derived from satellite measurements of tropospheric NO
759 2 columns. *Atmospheric Chemistry and Physics*, 13, 9415-9438
- 760 Brenninkmeijer, C.A., & Cai, D.S. (2016). Earth System Chemistry integrated Modelling (ESCiMo) with the Modular Earth
761 Submodel System (MESSy) version 2.51. *Geoscientific Model Development*, 9, 1153
- 762 Che, K., Cai, Z., Liu, Y., Wu, L., Yang, D., Chen, Y., Meng, X., Zhou, M., Wang, J., & Yao, L. (2022). Lagrangian inversion of
763 anthropogenic CO₂ emissions from Beijing using differential column measurements. *Environmental Research Letters*, 17,
764 075001
- 765 Che, K., Lauvaux, T., Taquet, N., Stremme, W., Xu, Y., Alberti, C., Lopez, M., García - Reynoso, A., Ciais, P., & Liu, Y. (2024).
766 CO₂ emissions estimate from Mexico City using ground - and space - based remote sensing. *Journal of Geophysical Research:
767 Atmospheres*, 129, e2024JD041297
- 768 Cheng, C., Liu, D., Wang, S., Zhang, X., Zhang, L., Chen, W., Liu, J., Wan, X., Chen, W., & Chen, X. (2025). Estimating strong
769 point CO₂ emissions by combining spaceborne IPDA lidar and HSRL. *Remote sensing of environment*, 328, 114898



- 770 Crippa, M., Guizzardi, D., Muntean, M., Schaaf, E., Dentener, F., Van Aardenne, J.A., Monni, S., Doering, U., Olivier, J.G., &
771 Pagliari, V. (2018). Gridded emissions of air pollutants for the period 1970–2012 within EDGAR v4. 3.2. *Earth Syst. Sci. Data*,
772 10, 1987-2013
- 773 Dai, G., Wu, S., Long, W., Liu, J., Xie, Y., Sun, K., Meng, F., Song, X., Huang, Z., & Chen, W. (2024). Aerosol and cloud data
774 processing and optical property retrieval algorithms for the spaceborne ACDL/DQ-1. *Atmospheric Measurement Techniques*,
775 17, 1879-1890
- 776 Danielson, J.J., & Gesch, D.B. (2011). Global multi-resolution terrain elevation data 2010 (GMTED2010). In: US Geological Survey
- 777 Dickerson, R.R., Stedman, D.H., & Delany, A.C. (1982). Direct measurements of ozone and nitrogen dioxide photolysis rates in the
778 troposphere. *Journal of Geophysical Research: Oceans*, 87, 4933-4946
- 779 Eldering, A., Wennberg, P., Crisp, D., Schimel, D., Gunson, M., Chatterjee, A., Liu, J., Schwandner, F., Sun, Y., & O'dell, C. (2017).
780 The Orbiting Carbon Observatory-2 early science investigations of regional carbon dioxide fluxes. *Science*, 358, eaam5745
- 781 Eskes, H., van Geffen, J., Sneep, M., Veeffkind, P., Niemeijer, S., & Zehner, C. (2021). S5P Nitrogen Dioxide v02. 03.01 intermediate
782 reprocessing on the S5P-PAL system: Readme file. In, ESA (p. 12)
- 783 Feng, S., Jiang, F., Wang, H., Liu, Y., He, W., Wang, H., Shen, Y., Zhang, L., Jia, M., & Ju, W. (2024). China's fossil fuel CO₂
784 emissions estimated using surface observations of coemitted NO₂. *Environmental Science & Technology*, 58, 8299-8312
- 785 Gately, C.K., & Hutyrá, L.R. (2017). Large uncertainties in urban - scale carbon emissions. *Journal of Geophysical Research:*
786 *Atmospheres*, 122, 11,242-211,260
- 787 Hakkarainen, J., Ialongo, I., & Tamminen, J. (2016). Direct space - based observations of anthropogenic CO₂ emission areas from
788 OCO - 2. *Geophysical Research Letters*, 43, 11,400-411,406
- 789 Han, G., Huang, Y., Shi, T., Zhang, H., Li, S., Zhang, H., Chen, W., Liu, J., & Gong, W. (2024). Quantifying CO₂ emissions of
790 power plants with Aerosols and Carbon Dioxide Lidar onboard DQ-1. *Remote sensing of environment*, 313, 114368
- 791 Han, G., Ma, X., Liang, A., Zhang, T., Zhao, Y., Zhang, M., & Gong, W. (2017). Performance evaluation for China's planned CO₂-
792 IPDA. *Remote Sensing*, 9, 768
- 793 Han, G., Zhang, H., Huang, Y., Chen, W., Mao, H., Zhang, X., Ma, X., Li, S., Zhang, H., & Liu, J. (2025). First global XCO₂
794 observations fromspaceborne lidar: methodology and initial result. *Remote sensing of environment*, 330, 114954
- 795 Hersbach, H., Bell, B., Berrisford, P., Biavati, G., Horányi, A., Muñoz Sabater, J., Nicolas, J., Peubey, C., Radu, R., & Rozum, I.
796 (2023). ERA5 hourly data on single levels from 1940 to present. Copernicus climate change service (c3s) climate data store
797 (cds), 10
- 798 Huang, T., Zhu, X., Zhong, Q., Yun, X., Meng, W., Li, B., Ma, J., Zeng, E.Y., & Tao, S. (2017). Spatial and temporal trends in global
799 emissions of nitrogen oxides from 1960 to 2014. *Environmental Science & Technology*, 51, 7992-8000
- 800 Huang, Y., Han, G., Shi, T., Li, S., Mao, H., Nie, Y., & Gong, W. (2024). Fi-scape: a divergence theorem based emission



- 801 quantification model for air/space-borne imaging spectrometer derived xch4 observations. *IEEE Journal of Selected Topics in*
802 *Applied Earth Observations and Remote Sensing*
- 803 Kiemle, C., Ehret, G., Amediek, A., Fix, A., Quatrevalet, M., & Wirth, M. (2017). Potential of spaceborne lidar measurements of
804 carbon dioxide and methane emissions from strong point sources. *Remote Sensing*, 9, 1137
- 805 Kiemle, C., Quatrevalet, M., Ehret, G., Amediek, A., Fix, A., & Wirth, M. (2011). Sensitivity studies for a space-based methane
806 lidar mission. *Atmospheric Measurement Techniques*, 4, 2195-2211
- 807 Koene, E.F.M., Brunner, D., & Kuhlmann, G. (2024). On the theory of the divergence method for quantifying source emissions
808 from satellite observations. *Journal of Geophysical Research: Atmospheres*, 129, e2023JD039904
- 809 Köhler, P., Guanter, L., Kobayashi, H., Walther, S., & Yang, W. (2018). Assessing the potential of sun-induced fluorescence and the
810 canopy scattering coefficient to track large-scale vegetation dynamics in Amazon forests. *Remote sensing of environment*, 204,
811 769-785
- 812 Konovalov, I.B., Berezin, E.V., Ciais, P., Broquet, G., Zhuravlev, R.V., & Janssens-Maenhout, G. (2016). Estimation of fossil-fuel
813 CO₂ emissions using satellite measurements of "proxy" species. *Atmospheric Chemistry and Physics*, 16, 13509-13540
- 814 Le Quéré, C., Andrew, R.M., Friedlingstein, P., Sitch, S., Hauck, J., Pongratz, J., Pickers, P.A., Korsbakken, J.I., Peters, G.P., &
815 Canadell, J.G. (2018). Global carbon budget 2018. *Earth System Science Data*, 10, 2141-2194
- 816 Li, X., Xiao, J., & He, B. (2018). Chlorophyll fluorescence observed by OCO-2 is strongly related to gross primary productivity
817 estimated from flux towers in temperate forests. *Remote sensing of environment*, 204, 659-671
- 818 Lin, J., & Gerbig, C. (2005). Accounting for the effect of transport errors on tracer inversions. *Geophysical Research Letters*, 32
- 819 Liu, F., Duncan, B.N., Krotkov, N.A., Lamsal, L.N., Beirle, S., Griffin, D., McLinden, C.A., Goldberg, D.L., & Lu, Z. (2020). A
820 methodology to constrain carbon dioxide emissions from coal-fired power plants using satellite observations of co-emitted
821 nitrogen dioxide. *Atmospheric Chemistry and Physics*, 20, 99-116
- 822 Liu, M., Van Der A, R., Van Weele, M., Eskes, H., Lu, X., Veeffkind, P., De Laat, J., Kong, H., Wang, J., & Sun, J. (2021). A new
823 divergence method to quantify methane emissions using observations of Sentinel - 5P TROPOMI. *Geophysical Research*
824 *Letters*, 48, e2021GL094151
- 825 Miller, J.B., Tans, P.P., & Gloor, M. (2014). Steps for success of OCO-2. *Nature Geoscience*, 7, 691-691
- 826 Oda, T., Bun, R., Kinakh, V., Topylko, P., Halushchak, M., Marland, G., Lauvaux, T., Jonas, M., Maksyutov, S., & Nahorski, Z.
827 (2019). Errors and uncertainties in a gridded carbon dioxide emissions inventory. *Mitigation and Adaptation Strategies for*
828 *Global Change*, 24, 1007-1050
- 829 Oda, T., & Maksyutov, S. (2015). ODIAC Fossil Fuel CO₂ Emissions Dataset (version: ODIAC2020b). Center for Global
830 Environmental Research, National Institute for Environmental Studies [data set], <https://doi.org/10.17595/20170411.001>
- 831 Qin, K., Lu, L., Liu, J., He, Q., Shi, J., Deng, W., Wang, S., & Cohen, J.B. (2023). Model-free daily inversion of NO_x emissions



- 832 using TROPOMI (MCMFE-NO_x) and its uncertainty: Declining regulated emissions and growth of new sources. *Remote*
833 *sensing of environment*, 295, 113720
- 834 Refaat, T.F., Singh, U.N., Yu, J., Petros, M., Remus, R., & Ismail, S. (2016). Double-pulse 2- μ m integrated path differential
835 absorption lidar airborne validation for atmospheric carbon dioxide measurement. *Applied Optics*, 55, 4232-4246
- 836 Reuter, M., Buchwitz, M., Schneising, O., Krautwurst, S., O'Dell, C.W., Richter, A., Bovensmann, H., & Burrows, J.P. (2019).
837 Towards monitoring localized CO₂ emissions from space: co-located regional CO₂ and NO₂ enhancements observed by the
838 OCO-2 and SSP satellites. *Atmospheric Chemistry and Physics*, 19, 9371-9383
- 839 Rey-Pommier, A., Chevallier, F., Ciais, P., Christoudias, T., Kushta, J., Georgiou, G., Violaris, A., Dubart, F., & Sciare, J. (2025).
840 Mapping NO_x emissions in Cyprus using TROPOMI observations: evaluation of the flux-divergence scheme using multiple
841 parameter sets. *Environmental Science and Pollution Research*, 32, 1932-1951
- 842 Schwandner, F.M., Gunson, M.R., Miller, C.E., Carn, S.A., Eldering, A., Krings, T., Verhulst, K.R., Schimel, D.S., Nguyen, H.M.,
843 & Crisp, D. (2017). Spaceborne detection of localized carbon dioxide sources. *Science*, 358, eaam5782
- 844 Sheng, M., Hou, Y., Song, H., Ye, X., Lei, L., Ma, P., & Zeng, Z.-C. (2025). Estimating anthropogenic CO₂ emissions from China's
845 Yangtze River Delta using OCO-2 observations and WRF-Chem simulations. *Remote sensing of environment*, 316, 114515
- 846 Sun, K. (2022). Derivation of emissions from satellite - observed column amounts and its application to TROPOMI NO₂ and CO
847 observations. *Geophysical Research Letters*, 49, e2022GL101102
- 848 Sun, K., Li, L., Jagini, S., & Li, D. (2021). A Satellite Data-Driven Framework to Rapidly Quantify Air Basin-Scale NO_x Emission
849 and Its Application to the Po Valley during the COVID-19 Pandemic. *Atmospheric Chemistry and Physics Discussions*, 2021,
850 1-29
- 851 Sun, K., Zhu, L., Cady-Pereira, K., Chan Miller, C., Chance, K., Clarisse, L., Coheur, P.-F., González Abad, G., Huang, G., & Liu,
852 X. (2018a). A physics-based approach to oversample multi-satellite, multispecies observations to a common grid. *Atmospheric*
853 *Measurement Techniques*, 11, 6679-6701
- 854 Sun, Y., Frankenberg, C., Jung, M., Joiner, J., Guanter, L., Köhler, P., & Magney, T. (2018b). Overview of Solar-Induced chlorophyll
855 Fluorescence (SIF) from the Orbiting Carbon Observatory-2: Retrieval, cross-mission comparison, and global monitoring for
856 GPP. *Remote sensing of environment*, 209, 808-823
- 857 Team, M. (2012). The Multi-resolution Emission Inventory Model for Climate and Air Pollution Research, MEIC Model [data set].
858 In
- 859 Van Geffen, J., Eskes, H., Compernelle, S., Pinardi, G., Verhoelst, T., Lambert, J.-C., Sneep, M., Ter Linden, M., Ludewig, A., &
860 Boersma, K.F. (2022). Sentinel-5P TROPOMI NO₂ retrieval: impact of version v2. 2 improvements and comparisons with
861 OMI and ground-based data. *Atmospheric Measurement Techniques*, 15, 2037-2060
- 862 Veeffkind, J.P., Aben, I., McMullan, K., Förster, H., De Vries, J., Otter, G., Claas, J., Eskes, H., De Haan, J., & Kleipool, Q. (2012).



- 863 TROPOMI on the ESA Sentinel-5 Precursor: A GMES mission for global observations of the atmospheric composition for
864 climate, air quality and ozone layer applications. *Remote sensing of environment*, 120, 70-83
- 865 Wang, J., Kawa, S., Eluszkiewicz, J., Baker, D., Mountain, M., Henderson, J., Nehrkorn, T., & Zaccheo, T. (2014). A regional CO
866 2 observing system simulation experiment for the ASCENDS satellite mission. *Atmospheric Chemistry and Physics*, 14, 12897-
867 12914
- 868 Wang, R., Tao, S., Ciais, P., Shen, H., Huang, Y., Chen, H., Shen, G., Wang, B., Li, W., & Zhang, Y. (2013). High-resolution mapping
869 of combustion processes and implications for CO₂ emissions. *Atmospheric Chemistry and Physics*, 13, 5189-5203
- 870 Wei, C. (2024). Historical trend and drivers of China's CO₂ emissions from 2000 to 2020. *Environment, development and*
871 *sustainability*, 26, 2225-2244
- 872 Wu, D., Lin, J.C., Fasoli, B., Oda, T., Ye, X., Lauvaux, T., Yang, E.G., & Kort, E.A. (2018). A Lagrangian approach towards
873 extracting signals of urban CO₂ emissions from satellite observations of atmospheric column CO₂ (XCO₂): X-Stochastic
874 Time-Inverted Lagrangian Transport model ("X-STILT v1"). *Geoscientific Model Development*, 11, 4843-4871
- 875 Xu, J., Guan, Y., Oldfield, J., Guan, D., & Shan, Y. (2024). China carbon emission accounts 2020-2021. *Applied Energy*, 360, 122837
- 876 Xu, T., Zhang, C., & Liu, C. (2025). Enhanced quantification of global carbon emitters using collocated OCO - 3 CO₂ and NO₂
877 observations from twin polar - orbiting satellites. *Geophysical Research Letters*, 52, e2025GL116877
- 878 Yang, E.G., Kort, E.A., Ott, L.E., Oda, T., & Lin, J.C. (2023). Using space - based CO₂ and NO₂ observations to estimate urban
879 CO₂ emissions. *Journal of Geophysical Research: Atmospheres*, 128, e2022JD037736
- 880 Ye, X., Lauvaux, T., Kort, E.A., Oda, T., Feng, S., Lin, J.C., Yang, E.G., & Wu, D. (2020). Constraining fossil fuel CO₂ emissions
881 from urban area using OCO - 2 observations of total column CO₂. *Journal of Geophysical Research: Atmospheres*, 125,
882 e2019JD030528
- 883 Yi, J., Huang, Y., Pei, Z., & Han, G. (2024). Urban area observing system (UAOS) simulation experiment using DQ-1 total column
884 concentration observations. *EGUsphere*, 2024, 1-40
- 885 Zhang, Q., Boersma, K.F., Zhao, B., Eskes, H., Chen, C., Zheng, H., & Zhang, X. (2022). Quantifying daily NO_x and CO₂
886 emissions from Wuhan using satellite observations from TROPOMI and OCO-2. *Atmospheric Chemistry and Physics*
887 *Discussions*, 2022, 1-18
- 888 Zhang, Q., Streets, D.G., Carmichael, G.R., He, K., Huo, H., Kannari, A., Klimont, Z., Park, I., Reddy, S., & Fu, J. (2009). Asian
889 emissions in 2006 for the NASA INTEX-B mission. *Atmospheric Chemistry and Physics*, 9, 5131-5153
- 890 Zhang, X., Yang, H., Bu, L., Fan, Z., Xiao, W., Chen, B., Zhang, L., Liu, S., Wang, Z., & Liu, J. (2025). Estimation of diurnal
891 emissions of CO₂ from thermal power plants using spaceborne integrated path differential absorption (IPDA) lidar.
892 *Atmospheric Chemistry and Physics*, 25, 6725-6740
- 893 Zheng, B., Geng, G., Ciais, P., Davis, S.J., Martin, R.V., Meng, J., Wu, N., Chevallier, F., Broquet, G., & Boersma, F. (2020).



894 Satellite-based estimates of decline and rebound in China's CO₂ emissions during COVID-19 pandemic. *Science advances*, 6,
895 eabd4998
896